Neuron

Microglia regulate neuronal activity via structural remodeling of astrocytes

Highlights

- A high-salt diet induces accumulation of reactive microglia around vasopressin neurons
- Reactive microglia prune astrocytic processes surrounding vasopressin neurons
- Astrocyte pruning leads to glutamate spillover, increasing vasopressin neuron activity
- Microglia-mediated increases in neuronal activity lead to salt-dependent hypertension

Authors

Ning Gu, Olena Makashova, Celeste Laporte, ..., Arkady Khoutorsky, Charles W. Bourque, Masha Prager-Khoutorsky

Correspondence

masha.prager-khoutorsky@mcgill.ca

In brief

Gu et al. showed that in rats fed a high-salt diet, reactive microglia accumulate around vasopressin-secreting neurons, phagocytosing astrocytic elements and pruning astrocytes. This causes glutamate spillover, increased neuronal activity, and excessive vasopressin release, contributing to salt-induced hypertension. The study reveals a novel mechanism by which microglia regulate synaptic transmission and neuronal activity through structural remodeling of astrocytes in the adult brain.



Neuron



Article

Microglia regulate neuronal activity via structural remodeling of astrocytes

Ning Gu,¹ Olena Makashova,¹ Celeste Laporte,¹ Chris Qilongyue Chen,¹ Banruo Li,¹ Pierre-Marie Chevillard,¹ Graham Lean,¹ Jieyi Yang,¹ Calvin Wong,² Jonathan Fan,² Behrang Sharif,³ Susana Puche Saud,¹ Misha Hubacek,¹ Katrina Y. Choe,⁴ Margaret M. McCarthy,⁵ Arkady Khoutorsky,² Charles W. Bourque,⁶ and Masha Prager-Khoutorsky¹.√,⁵

¹Department of Physiology, McIntyre Medical Sciences Building, McGill University, Montreal, QC, Canada

SUMMARY

Neuron-glia interactions play a central role in regulating synaptic transmission and neuronal excitability. The structural plasticity of astrocytes is associated with numerous physiological and pathological conditions; however, the mechanism underlying this process remains unknown. To examine the basis for structural astrocyte plasticity, we used the classic example of the loss of astrocytic processes that takes place in the rat hypothalamic magnocellular system during chronic high-salt intake. We discovered that a high-salt diet triggers a local accumulation of reactive microglia around vasopressin-secreting neurons but not in other brain areas. Microglia phagocytose astrocytic processes, reducing astrocytic coverage of vasopressin neurons. The pruning of astrocytic processes impairs synaptic glutamate clearance, enabling activation of extrasynaptic glutamate NMDA receptors and increasing the activity of vasopressin neurons. Inhibiting microglia-mediated astrocyte pruning attenuates the increased neuronal activity and vasopressin-dependent hypertensive phenotype of rats fed a high-salt diet. Thus, microglia orchestrate neuron-glia interactions and regulate neuronal activity through astrocyte pruning.

INTRODUCTION

Neuron-glia interactions are crucial for regulating neuronal activity to control brain function in physiological and pathological conditions. The for example, astrocytes play a central role in modulating synaptic transmission, neurotransmitter clearance, and synaptic plasticity. Therefore, the structural remodeling of astrocytes, which occurs under various conditions, can strongly influence neural activity.

One of the classical systems where the structural plasticity of astrocytes and its functional outcomes have been investigated is the magnocellular hypothalamo-neurohypophysial system comprising supraoptic (SON) and paraventricular (PVN) nuclei, harboring magnocellular neurons releasing vasopressin (VP) or oxytocin. A striking feature of the astrocytes surrounding magnocellular neurons in the SON and PVN is their ability to undergo robust remodeling in response to the animal's physiological state demanding large and sustained increases in hormonal release. This plasticity is characterized by the reversible withdrawal of astrocytic processes that envelop magnocellular

neuron somata and dendrites, resulting in an increased number of direct soma-to-soma appositions, as well as a higher number of synapses. Previous studies have demonstrated a significant reduction in astrocytic coverage of oxytocin neurons during lactation and chronic dehydration, indicating that this structural plasticity facilitates and/or makes hormonal release more efficient. It has also been described in dehydration caused by water deprivation, supporting sustained increases in VP secretion to concentrate urine and minimize water loss when an animal has limited access to water, as well as following exposure to a high-salt diet (HSD). If Although this remarkable plasticity was first documented nearly five decades ago, T-20 the mechanism underlying this process remains unknown, and our understanding of its role is still incomplete.

Here, we addressed these questions by examining astrocyte structural plasticity in response to HSD. We used rats for this study, as mice are less suitable for investigating central adaptations in fluid balance. As desert-adapted animals, mice have more efficient renal mechanisms for water retention and urine concentration than rats or humans, 21–24 making them more

²Department of Anesthesia, Alan Edwards Centre for Research on Pain, Faculty of Dental Medicine and Oral Health Sciences, McGill University, Montreal, QC, Canada

³Department of Neurology & Neurosurgery, McGill University, Montreal, QC, Canada

⁴Department of Psychology, Neuroscience & Behaviour, McMaster University, Hamilton, ON, Canada

⁵Department of Pharmacology and Physiology, University of Maryland School of Medicine, Baltimore, MD, USA

⁶Brain Repair and Integrative Neuroscience Program, Research Institute of the McGill University Health Centre, Montreal, QC, Canada ⁷Lead contact

^{*}Correspondence: masha.prager-khoutorsky@mcgill.ca https://doi.org/10.1016/j.neuron.2025.07.024





resistant to dehydration and fluid balance perturbations. ^{25–28} Thus, mice show minimal changes in plasma osmolality or blood pressure responses even after prolonged high-salt intake. ^{29–31} Rats exhibit fluid regulation patterns more similar to humans, making them a more appropriate model for studying astrocyte responses to fluid balance challenges.

We found that astrocyte remodeling is mediated by reactive microglia, which phagocytose astrocytic processes surrounding magnocellular VP neurons. This leads to impaired astrocytic glutamate clearance and enhanced activation of extrasynaptic NMDA glutamate receptors, thus contributing to increased activation of VP neurons and VP-dependent elevation in blood pressure. Inhibiting microglia-mediated pruning of astrocytes attenuates changes in VP neuron activity and HSD-induced hypertension in rats, uncovering a new mechanism by which microglia orchestrate structural plasticity and neuron-glia interactions.

RESULTS

High-salt intake induces loss of astrocyte processes

To analyze astrocyte structural plasticity in the magnocellular system we exposed rats to HSD for 7 days by adding 2% NaCl to their drinking water. Consistent with previous ultrastructural studies, 8,9,17-20,32,33 immunohistochemical examination of the magnocellular system in rats fed HSD revealed a substantial decrease in astrocytic coverage, as visualized by glial fibrillary acidic protein (GFAP) in the SON (Figure 1A) and PVN (Figures S1A and S1B). To confirm this observation, we evaluated additional astrocytic markers, including S100 calciumbinding protein β (S100β), aldehyde dehydrogenase 1 family member L1 (ALDH1L1), glutamate transporter 1 (GLT1), and vimentin (Figures 1B-1E). Our data show reduced immunolabeling of these astrocytic proteins in the SON of rats fed HSD (Figures 1F-1J). The HSD-mediated decrease in astrocytic coverage was further validated by western blot analysis, which showed reduced levels of the astrocytic proteins GFAP, GLT1, and ALDH1L1 in the SON of rats fed HSD compared with a control diet (Figures S1C and S1D). A significant decrease in astrocytic coverage is observed as early as 5 days but not at 2 days after exposing rats to HSD (Figures S2A and S2B). Notably, the total number and density of astrocyte cell bodies in the SON and PVN remain unchanged after HSD (Figures S2C and S2D), suggesting that HSD does not cause the elimination of astrocytes but rather triggers a reduction in astrocytic processes surrounding magnocellular VP neurons.

High-salt intake causes accumulation of reactive microglia around VP neurons

Previous studies postulated that decreased astrocytic coverage is mediated by astrocyte retraction, ^{6,8,17,19,20,34} however evidence supporting this notion has been lacking. Microglia are the main immune cell type in the central nervous system (CNS) and have the capacity to engulf and phagocytose cellular elements. ^{35,36} Therefore, we hypothesized that microglia engulf astrocytic processes in HSD. To test this hypothesis, we examined the effect of HSD on microglial organization in the SON and PVN of rats. We found that Iba1-positive microglia accumulate in the

SON and PVN of HSD-fed animals but not in the surrounding areas (Figure 2A). Since Iba1 is expressed not only by microglia but also by macrophages, we used both Iba1 and the pan-microglial marker TMEM119 to confirm that HSD increases the density of microglia around VP neurons (Figures 2B-2G). In addition to the increased density of microglia around VP neurons in HSD (Figures 2A, 2E-2G, and S3A-S3C), the HSD induced changes in microglial morphology from a highly ramified shape with multiple thin branches to a less-complex morphology with shorter and thicker processes (Figure 2D), indicative of their activation.³⁷ Sholl analysis was used to quantify these changes in microglial morphology, showing a significant decrease in the number of Sholl intersections in microglia from HSD-treated rats (Figure 2H). These changes in microglial morphology appeared gradually. While very minor, non-significant alterations might appear as early as 2 days after exposing rats to HSD, significant changes in microglial morphology were only detected after 5 days, with microglia progressively acquiring a more reactive phenotype by 7 days of HSD (Figure S3D). Notably, while reactive microglia accumulated around VP neurons in the SON and PVN, their density and morphology remained unchanged outside these nuclei, where microglia remained in a "resting/naive" state (Figure S4). These results demonstrate that feeding rats HSD triggers the local accumulation of reactive microglia in brain nuclei containing magnocellular VP neurons.

Microglial inhibition attenuates HSD-induced loss of astrocyte processes

To study whether microglia play a role in the loss of astrocytic processes around magnocellular VP neurons, we inhibited microglia using pharmacological agents and examined if this prevents the loss of astrocytic processes induced by HSD. To inhibit microglia, we used PLX3397, an inhibitor of the colony-stimulating factor 1 receptor (CSF1R), a key regulator of microglial proliferation, activation, and survival. 38,39 The rats were administered PLX3397 (30 mg/kg/day intraperitoneally [i.p.]) or the vehicle daily for 3 days, then exposed to either the control diet or HSD for an additional 7 days, with PLX3397 administration continuing throughout the dietary protocols (for a total of 10 days). The treatment of rats fed HSD with PLX3397, but not the vehicle, prevented the accumulation of reactive microglia and blocked the loss of astrocytic processes around VP neurons (Figure S5).

To further confirm these observations, we used an additional CSF1R inhibitor, PLX5622, which is less effective overall but more specific in targeting CSF1R, ⁴⁰ with a 10-fold lower affinity for related kinases compared with PLX3397, ⁴¹ and is therefore considered more efficient in depleting microglia. ^{40,41} The rats were administered with either the vehicle or PLX5622 (twice a day, for a total of 100 mg/kg/day i.p.) for 3 days, after which PLX5622 or vehicle injections continued during exposure to HSD or the control diet. The treatment of HSD-fed rats with PLX5622, but not the vehicle, not only prevented the accumulation of reactive microglia but decreased their density compared with the control (Figures S6A–S6C). Similar to PLX3397, treatment of HSD-fed rats with PLX5622 also inhibited the loss of astrocytic processes around VP neurons (Figures S6A and S6D).





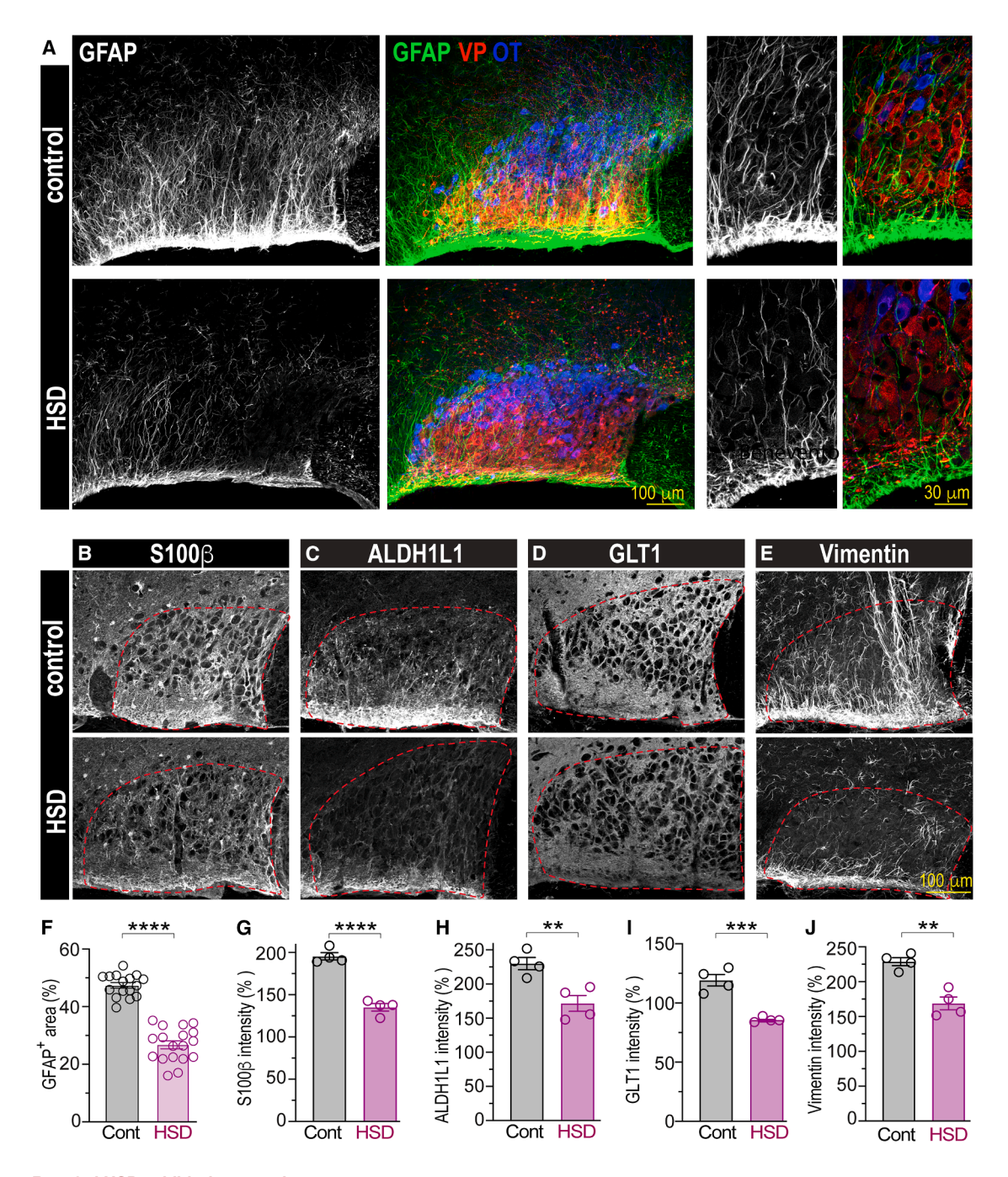


Figure 1. Rats fed HSD exhibit decreased astrocyte coverage

(A–E) Coronal rat brain sections immunolabeled to visualize astrocytes (GFAP, white or green) and neurons secreting VP (red) or oxytocin (blue) in the SON of control rats (top) or rats fed HSD (7 days of 2% NaCl in the drinking solution, bottom). Additional astrocytic markers S100 β (B), ALDH1L1 (C), GLT1 (D), and vimentin (E) visualized in the SON of rats fed the control diet (upper) and HSD (bottom). Red dotted lines outline VP neuron location. (F) Quantification of GFAP in the SON of rats fed the control diet or HSD (n = 16 control, n = 18 HSD rats).

(G–J) Quantifications of S100 β , ALDH1L1, GLT1, and vimentin in the SON of rats fed the control diet or HSD, n=4 rats/group. Data presented as mean \pm SEM, analyzed by Student's t test, ****p < 0.0001, ***p < 0.001, and **p < 0.01, each data point represents one rat. See also Figures S1 and S2.

Microglia are the only cell type expressing CSF1R in the CNS^{42,43}; however, systemic administration of CSF1R inhibitors can also affect peripheral macrophages.⁴⁴ Thus, to avoid effects

on peripheral macrophages and selectively target microglia in the CNS, we administered an additional CSF1R inhibitor, BLZ945, 45 directly into the brain. To this end, rats were



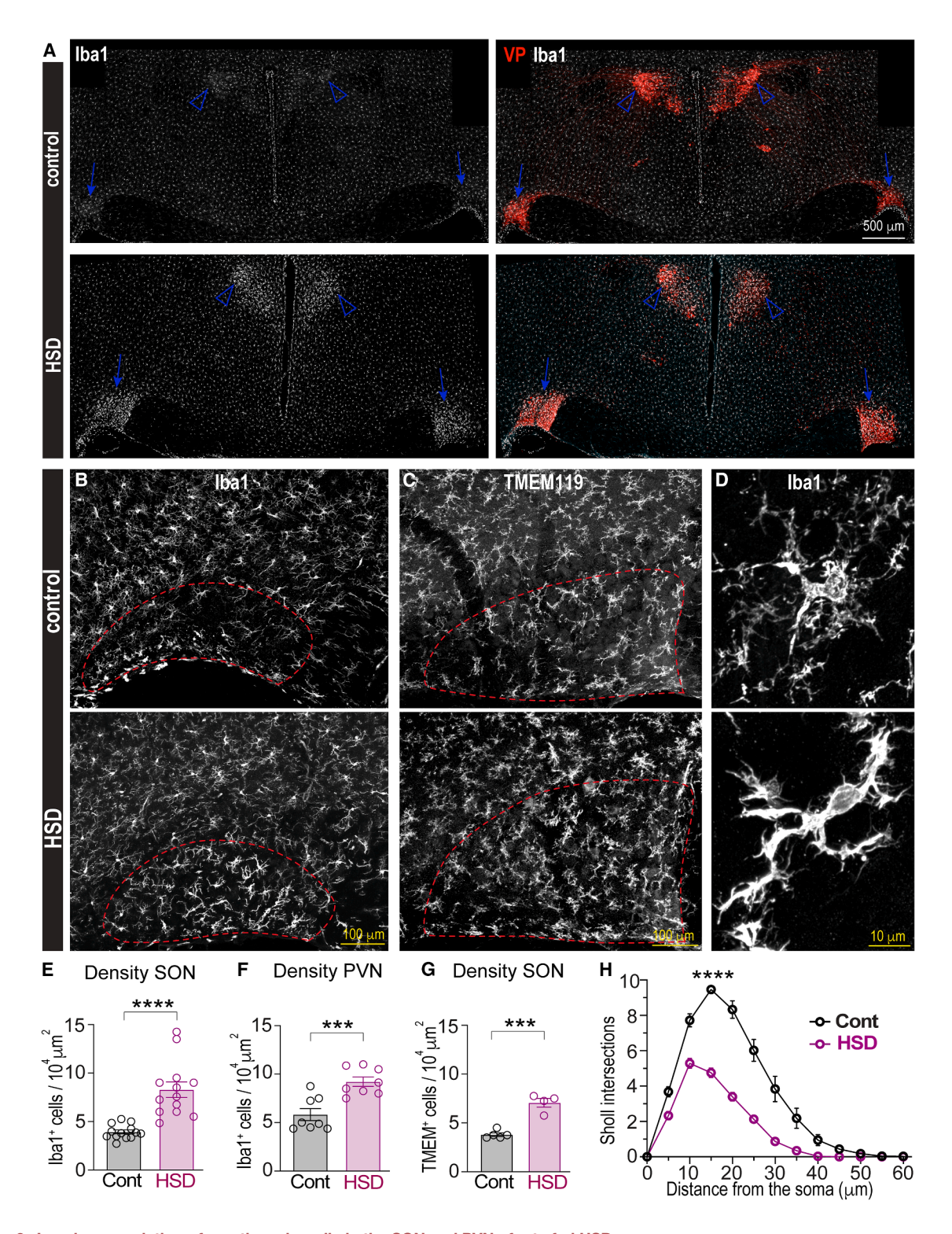


Figure 2. Local accumulation of reactive microglia in the SON and PVN of rats fed HSD

(A) Low-magnification images of hypothalamic brain sections showing Iba1-positive microglia (white) and VP neurons (red) in the SONs (arrows) and PVNs (arrowheads). Rats fed the control diet (upper) show a homogeneous distribution of microglia, while in HSD (bottom), microglia accumulate around VP neurons of the SON and PVN.

(B and C) Confocal images of SON sections from the control (upper) and HSD-treated (bottom) rats show Iba1- (B) and TMEM119-positive microglia (C), red dotted line outlines VP neuron location.

(legend continued on next page)

Neuron Article



implanted with an intracerebroventricular (i.c.v.) cannula in the lateral ventricle. Two weeks after recovery, they received daily i.c.v. injections of BLZ945 (0.3 mg/kg/day) or vehicle for 3 days. On the fourth day, rats were exposed to either the control diet or HSD for an additional 7 days, while daily BLZ945 administration continued throughout the dietary protocols. Treatment of HSD-fed rats with BLZ945, but not the vehicle, prevented the accumulation of microglia in the SON (Figures 3A-3C) and PVN (Figures S7A–S7C). BLZ945 treatment completely reversed HSD-induced changes in microglial morphology, suggesting that it prevented microglial activation in response to HSD (Figure 3D). Strikingly, this inhibition of microglia blocked the loss of the astrocytic marker GFAP around VP neurons of the SON (Figures 3A and 3E) and PVN (Figures S7A and S7D) of rats exposed to HSD. The effect of microglial inhibition on HSD-induced decreases in GFAP coverage was detected as early as 5 days after the initiation of the dietary protocol (Figure S8). Furthermore, in addition to GFAP, microglial inhibition with BLZ945 prevented the HSD-induced loss of all examined astrocytic markers in the SON, including S100ß, ALDH1L1, GLT1, and vimentin (Figures S9A-S9D). These data suggest that HSD-induced accumulation of reactive microglia mediates the reduction in astrocytic coverage around VP neurons in the SON and PVN.

Microglia phagocytose astrocytic processes during high-salt intake

Microglia phagocytose neuronal elements under various physiological conditions (e.g., developmental synaptic pruning and plasticity), ³⁵ as well as in disease states (e.g., multiple sclerosis, Alzheimer's disease). ^{36,46,47} Accordingly, the enhanced phagocytic capacity of reactive microglia is associated with an increased number of CD68-positive (CD68+) phagocytic lysosomes within microglia in the phagocytic state. Assessing CD68+ lysosomes has therefore been used to quantify the phagocytic capacity of microglia. ^{48,49}

To determine whether HSD stimulates microglia to become phagocytic and engulf astrocytic processes surrounding VP neurons, we analyzed whether microglia in this condition contain CD68+ lysosomes. Super-resolution imaging with Airyscan combined with 3D reconstruction of individual microglia using IMARIS revealed that the number of CD68+ lysosomes was higher in SON microglia from rats fed HSD compared with those on the control diet (Figures 4A–4C; Videos S1 and S2). Moreover, HSD significantly increased the volume occupied by phagocytic lysosomes within the microglial cytoplasm (Figure 4D). These HSD-induced increases in the number and volume of CD68+ lysosomes were abolished when rats were administered BLZ945 i. c.v. but not the vehicle (Figures 4A–4C; Video S3). Strikingly, 3D

colocalization analyses showed that most CD68+ lysosomes within SON microglia from HSD-fed rats contained astrocytic markers GFAP and S100β (Figures 4A, 4E, and 4F; Video S2). We found very little or no astrocytic components in microglia from rats fed the control diet. Additionally, BLZ945 inhibited HSD-induced increases in astrocytic material within microglial CD68+ lysosomes (Figures 4A, 4E, and 4F). To examine whether microglia in HSD-treated rats also engulf neuronal components, we analyzed if CD68+ lysosomes colocalize with the general pan-neuronal marker NeuN and VP, which is abundantly present in the dendrites of magnocellular VP neurons. Importantly, while most microglial CD68+ lysosomes contained significant amounts of astrocytic markers GFAP and S100 β in HSD (Figures 4E, 4F, and S10A), CD68+ lysosomes showed minimal colocalization with NeuN and VP in SON microglia in both the control and HSD-fed rats (Figures S10B and S10C). These results indicate that HSD stimulates microglial phagocytic activity, leading to the engulfment of astrocytic components and microglia-mediated pruning of astrocyte processes.

HSD-induced microglia-mediated pruning takes days *in vivo*; however, this slow time course likely reflects the gradual rise in osmolality in HSD. Previous studies showed that a reduction in astrocytic coverage can be induced *in vitro* within a few hours⁵⁰ or even minutes.⁵¹ To examine whether the microglia phagocytic response can be triggered by an acute hypertonic stimulus, we imaged microglia and astrocytes in acute SON slices from rats expressing enhanced green fluorescent protein (eGFP) in microglia⁵² and tdTomato in astrocytes. Following hypertonic stimulation, we occasionally observed astrocytic material colocalized with microglia, which appeared inside the microglia minutes later (Figure S11; Video S4). These events may represent phagocytosis of astrocytic material by microglia, consistent with our super-resolution imaging data showing astrocytic material inside microglial CD68+ lysosomes after chronic exposure to HSD.

Microglia-mediated pruning of astrocytic processes impairs synaptic glutamate clearance

Chronic hypertonic stimuli, such as HSD, enhance the osmosensitivity of magnocellular VP neurons⁵³ and increase their action potential firing *in vivo*. ⁵⁴ Whether changes in astrocyte coverage can contribute to this increased neuronal activity in HSD remains unclear. Previous studies showed that the degree of astrocytic coverage can govern the availability of transmitters in the extrasynaptic space, contributing to the regulation of synaptic efficacy and neuronal activation. ^{55,56} Our data show that the loss of astrocyte processes in HSD is manifested by decreased levels of several astrocytic proteins, including GLT1 (Figures 1I and S1D). Since GLT1 is the primary astrocytic glutamate transporter responsible for glutamate clearance in the synapse, ⁵⁷ we

See also Figures S3 and S4.

⁽D) High magnification Airyscan images illustrate HSD-induced changes in Iba1-positive microglial morphology from highly ramified in control (upper) to a less-complex shape with shorter and thicker processes, typical of reactive microglia in the SON from HSD rats (bottom).

⁽E–G) Quantification of Iba1-positive microglial density in the SON (E, n = 13 rats/group), PVN (F, n = 8 rats/group), and TMEM119-positive microglial density in the SON (G, n = 4 rats/group) in control or HSD rats, analyzed by Student's t test.

⁽H) Distribution of Sholl intersection number by the distance from microglial soma in the SONs from control and HSD rats (n = 5 rats/group, 20 cells per animal), p < 0.0001 by two-way ANOVA with Šídák's multiple comparisons post hoc test). Data presented as mean \pm SEM, ***p < 0.001 and ****p < 0.0001, each data point represents one rat.



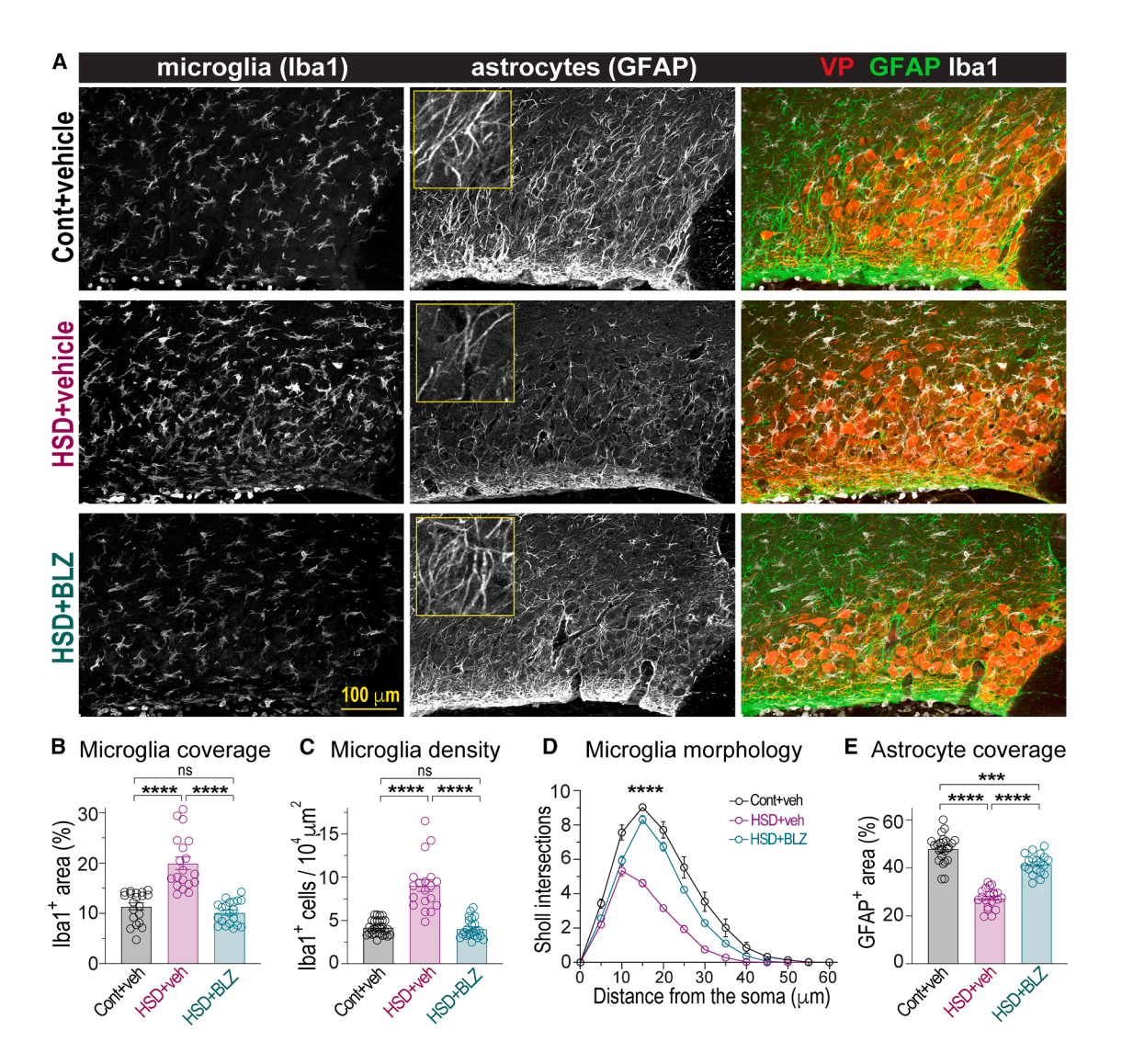


Figure 3. Microglial inhibition blocks astrocyte remodeling in HSD

(A–C) SON sections from control (cont) and HSD-fed rats treated with vehicle i.c.v. (veh), and HSD rats treated with 0.3 mg/kg/day BLZ945 i.c.v. (HSD + BLZ), labeled with markers of microglia (lba1), astrocytes (GFAP), and VP neurons. Quantification of microglial coverage, analyzed as lba1-immunopositive SON area (B), and microglial density (C) in rats exposed to different treatments (n = 19 rats/group, one-way ANOVA with Tukey's post hoc test).

(D) Distribution of Sholl intersection number by the distance from microglial soma in the SONs from vehicle-treated control and HSD-fed rats and BLZ-treated HSD rats (n = 5 rats/group, 20 cells per animal), p < 0.0001 by two-way ANOVA with Tukey's post hoc test.

(E) Astrocyte coverage analyzed as GFAP-immunopositive SON area in rats exposed to different treatments (n = 19 rats/group), one-way ANOVA with Tukey's post hoc, each point represents one rat.

See also Figures S5-S9.

hypothesized that in HSD, microglia-mediated astrocytic pruning impairs synaptic glutamate clearance by GLT1. As a result, spillover glutamate can activate extrasynaptic NMDA receptors (NMDARs) on VP neurons and induce a non-inactivating depolarizing current that contributes to the excitation of these neurons.

To test whether HSD-induced astrocyte pruning impairs the ability of GLT1 to regulate VP neuron activity, we performed whole-cell current-clamp recordings from VP neurons in hypothalamic slices. VP neurons were identified by their expression of eGFP. 60 Consistent with previous reports, pharmacological

inhibition of GLT1 with dihydrokainate (DHK), a specific inhibitor of GLT1, depolarized and increased the action potential firing rate of VP neurons in acute hypothalamic slices prepared from rats fed the control diet (Figures 5A and S12A). However, inhibiting GLT1 had no effect on VP neuron membrane potential and firing rate in slices prepared from rats fed HSD (Figures 5B and S12B). These results indicate that astrocytic GLT1 restricts the activity of VP neurons in the control condition, but this regulatory mechanism is lost in HSD. Notably, blocking microglia-mediated pruning of astrocytes by i.c.v. administration of BLZ945 throughout 7 days of HSD completely restored the effect of

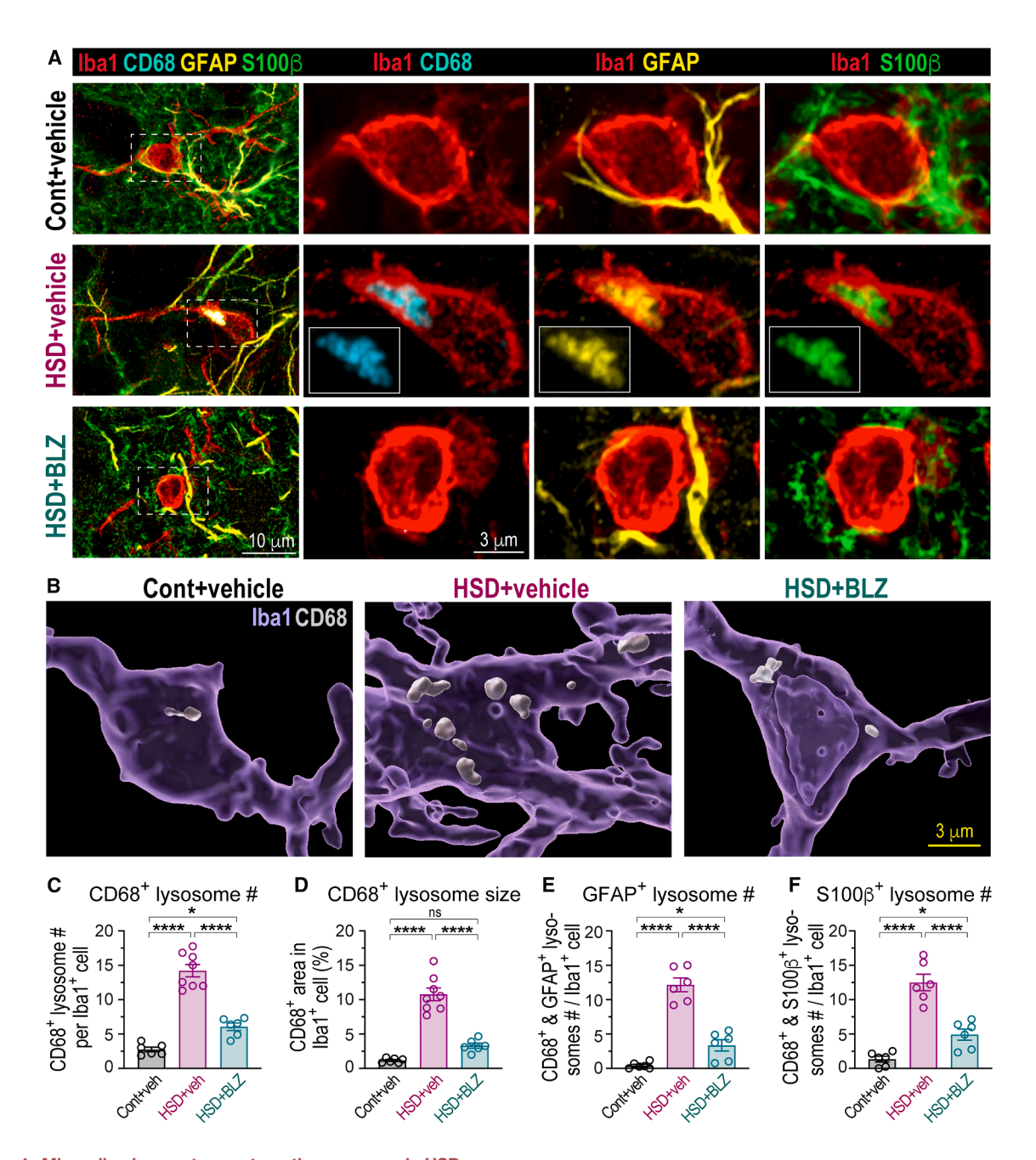


Figure 4. Microglia phagocytose astrocytic processes in HSD

(A) Super-resolution Airyscan images show microglia (Iba1, red), microglial-specific lysosomal marker CD68 (cyan), and astrocyte markers GFAP (yellow), and S100β (green) in the SONs from control (cont) and HSD-fed rats treated with vehicle i.c.v. (veh), and HSD rats treated with 0.3 mg/kg/day BLZ945 i.c.v. (HSD + BLZ).

(B–F) (B) IMARIS 3D surface reconstruction of microglia and CD68+ lysosomes from control and HSD-fed rats treated with BLZ945 or vehicle showing Iba1 (translucent purple), CD68 (opaque white); see also 3D reconstructions in Videos S1, S2, and S3. Bar graphs show the number of CD68+ lysosomes per microglia (C), the proportion of microglial area occupied by CD68+ lysosomes (D), and the number of CD68+ lysosomes colocalizing with GFAP (E) and S100 β (F) in above conditions, n = 6 rats/group, one-way ANOVA with Tukey's post hoc test. Data presented as mean \pm SEM; ****p < 0.0001 and *p < 0.05; ns, not significant; each data point represents one rat.

See also Figures S10 and S11 and Videos S1, S2, S3, and S4.

GLT1 inhibition by DHK on VP neuron excitability, while treating rats fed the control diet with BLZ945 had no effect on GLT1-mediated excitation of VP neurons (Figures 5C-5F and S12C-

S12F). These data demonstrate that microglia-mediated pruning of astrocytes in HSD hinders GLT1's capacity to prevent glutamate spillover. This impaired glutamate clearance by GLT1



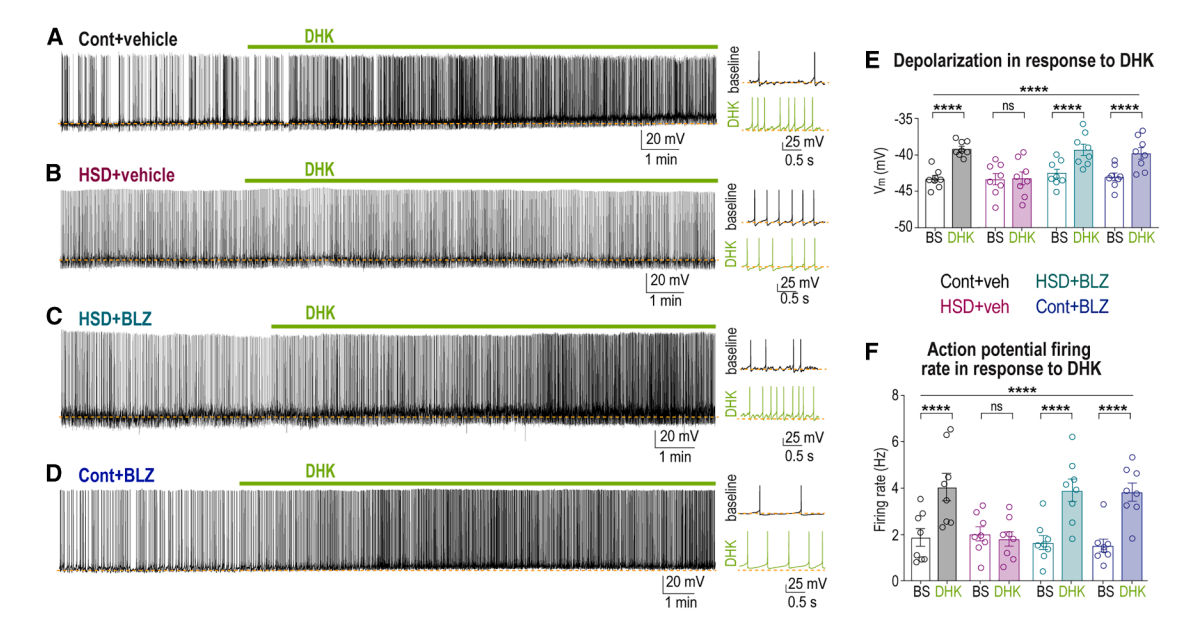


Figure 5. Microglia-mediated astrocyte pruning impairs synaptic glutamate clearance by astrocytic glutamate transporter (A–D) Left: sample current-clamp traces show the effect of bath application of glial glutamate transporter blocker DHK (100 μM, green bar) on action potential firing of VP neurons in SON brain slices prepared from vehicle-treated control (A) and HSD (B) rats and BLZ945-treated HSD (C) and control (D) rats. (E and F) Right: expanded 2-s sample traces before (black) and after (green) DHK application. Dashed lines show membrane potential at baseline. Bar graphs show changes in membrane potential (E) and firing rate (F) induced by DHK in SON VP neurons from vehicle-treated control and HSD and BLZ945-treated HSD and control rats (n = 8 rats/group, repeated measures two-way repeated measures ANOVA with Śidák's multiple comparisons post hoc test). Data presented as mean ± SEM; ****p < 0.0001; ns, not significant; each data point represents one rat.

results in spillover into the extrasynaptic space, which may activate extrasynaptic NMDARs.

HSD-induced impairment of synaptic glutamate clearance increases activation of extrasynaptic NMDARs

To examine whether impaired glutamate clearance contributes to an enhanced activation of extrasynaptic NMDARs in HSD, we measured persistent NMDAR-mediated currents in VP neurons from control and HSD-fed rats. To evaluate the contribution of tonic extrasynaptic NMDARs, we used ifenprodil, a selective blocker of NR2B NMDAR subunit (N-methyl-D-aspartate receptor subunit 2B),61 which is a predominant subunit comprising extrasynaptic NMDARs. 62,63 To assess the contribution of different glutamatergic currents, VP neurons from SON slices were voltage-clamped to +40 mV. The baseline holding current was recorded, along with changes in the holding current in response to the sequential bath application of drugs targeting different subsets of glutamate receptors. First, extrasynaptic NMDA currents were selectively blocked with ifenprodil. The remaining (synaptic) NMDA currents were then inhibited with AP-5 (2-amino-5-phosphonopentanoic acid). Finally, all residual non-NMDA glutamate receptors were blocked by applying the general blocker kynurenic acid (Figure 6A). Our results show that extrasynaptic NMDAR currents are significantly increased in VP neurons from HSD-fed rats compared with those on the control diet, and this increase was fully reversed by blocking microglia-mediated pruning of astrocytes with

BLZ945 (Figures 6A–6G). Also, we found that neither AP-5-sensitive currents, corresponding to synaptic ifenprodil-insensitive NMDARs, nor kynurenic acid, corresponding to non-NMDA (AMPA and kainate) currents, were altered in different treatments (Figures 6F and 6G). These data demonstrate that HSD leads to an increased availability of extrasynaptic NMDARs, and preventing microglia-mediated pruning of astrocytic processes in HSD reverses this increase.

To test whether the elevated tonic activation of extrasynaptic NMDARs contributes to increased excitability of VP neurons in rats fed HSD, we examined whether VP neuron activity is affected by blocking extrasynaptic NMDAR currents with ifenprodil. Current-clamp recordings from identified VP neurons showed that inhibiting extrasynaptic NMDAR currents has no effect on the activity of VP neurons from rats fed the control diet (Figures 6H, 6L, 6M, and S13A). However, blocking extrasynaptic NMDARs in VP neurons from HSD-fed animals hyperpolarized and reduced the action potential firing rate of these neurons (Figures 6I, 6L, 6M, and S13B), revealing the presence of tonic excitatory currents in this condition. Blocking microglia-mediated pruning of astrocytes in HSD with BLZ945 eliminated ifenprodil-sensitive inhibition, while treating rats fed the control diet with BLZ945 had no effect (Figures 6J-6M and S13C-S13F). These data indicate that microglia-mediated pruning of astrocytic processes impairs synaptic glutamate clearance, leading to the tonic activation of extrasynaptic glutamate receptors on magnocellular VP neurons and contributing to the elevated firing activity of VP neurons in HSD.



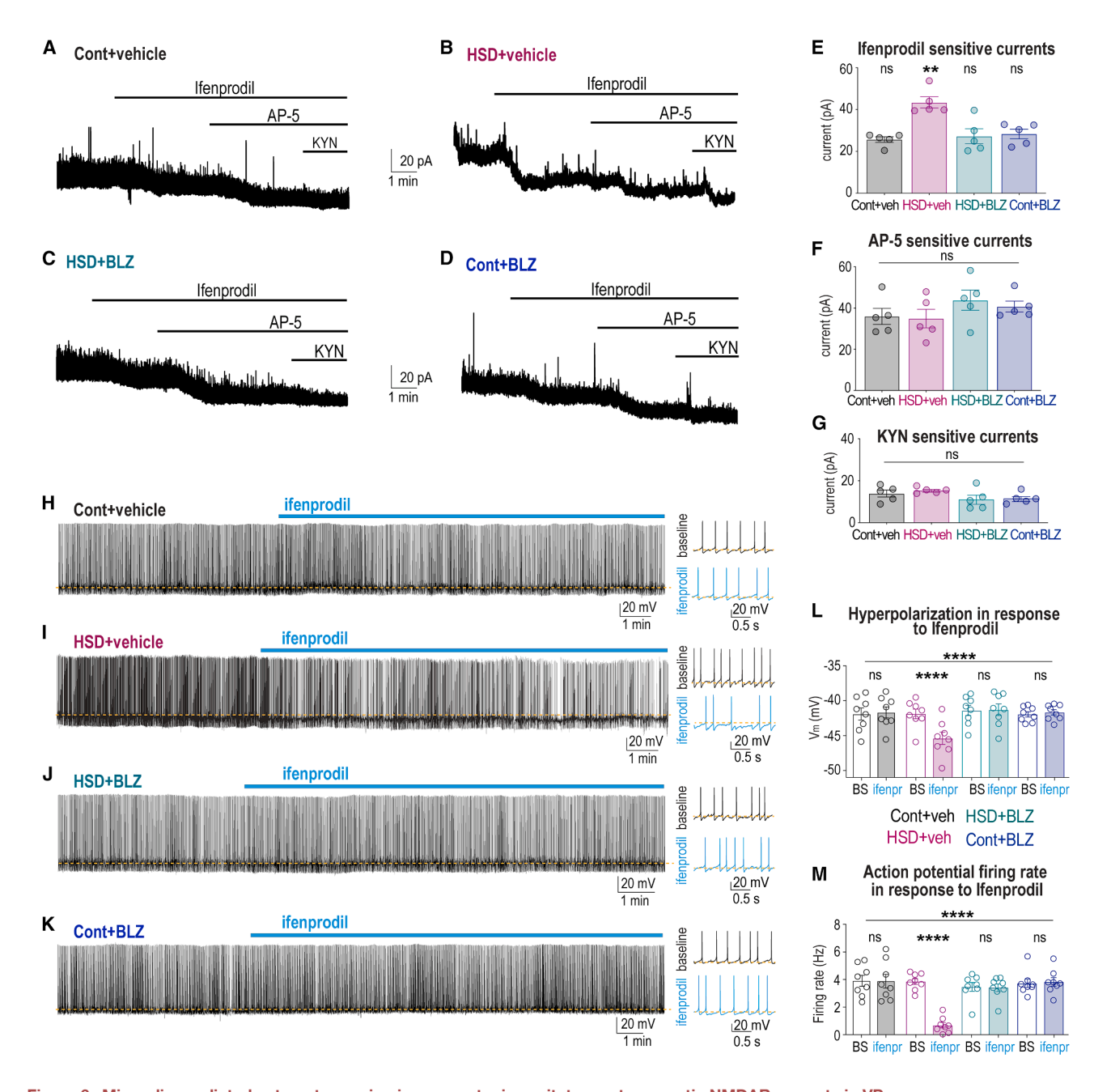


Figure 6. Microglia-mediated astrocyte pruning increases tonic excitatory extrasynaptic NMDAR currents in VP neurons

(A-G) (A-D) Sample traces showing the tonic NMDA current (I_{hold}) by sequential applications of ifenprodil (10 μ M), AP-5 (100 μ M), and kynurenic acid (1 mM) from voltage-clamped VP neurons (V_{hold} +40 mV) in SON brain slices obtained from vehicle-treated control (A) and HSD rats (B) and BLZ945-treated HSD (C) and control (D) rats. Bar graphs show changes in I_{hold} in response to the application of ifenprodil (E), AP-5 (F), and kynurenic acid (G), in VP neurons from vehicle- or BLZ945-treated control and HSD rats (5 rats per condition, one-way repeated measures ANOVA with Tukey's post hoc test).

(H–M) (H–K) Left: sample current-clamp traces show the effect of ifenprodil (10 μ M, blue bar) on action potential firing of VP neurons in SON slices from vehicle-treated control (H) and HSD (I) rats and BLZ945-treated HSD (J) and control (K) rats. Right: expanded 2-s sample traces before (black) and after (blue) ifenprodil application. Dashed lines show membrane potential at baseline. Bar graphs show changes in membrane potential (L) and firing rate (M) induced by ifenprodil in VP neurons in SON brain slices from vehicle or BLZ945-treated control and HSD rats (n=8 rats/group, repeated measures two-way ANOVA with Šídák's multiple comparisons post hoc test). Data presented as mean \pm SEM; ****p<0.0001 and **p<0.001; ns, not significant; each data point represents one rat. See also Figure S13.



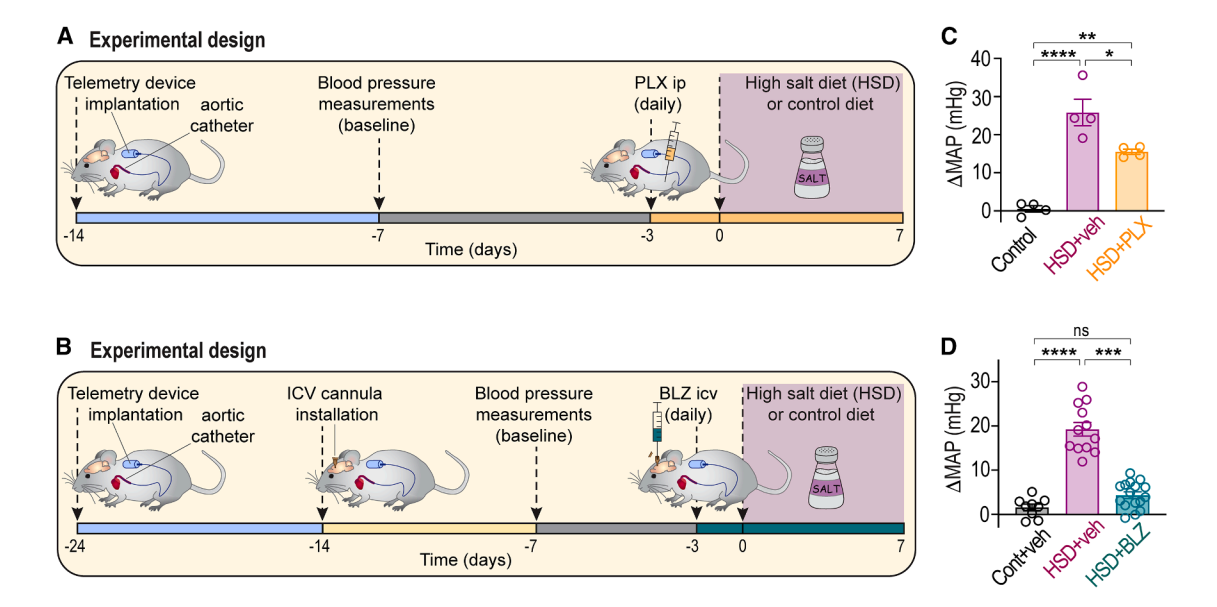


Figure 7. Blocking microglia-mediated astrocyte pruning prevents HSD-induced increases in blood pressure

(A and B) Schematic illustrations of the experimental design for blood pressure measurements in rats fed HSD and administered with PLX3397 i.p. (A) and BLZ945 i.c.v. (B).

(C) Bar graphs show changes in the mean arterial pressure (MAP) in rats fed control diet or HSD and treated with 30 mg/kg/day PLX3397 or vehicle i.p. daily (n = 4 rats/group).

(D) Bar graphs show changes in the MAP in rats fed control diet or HSD and treated with 0.3 mg/kg/day BLZ945 or vehicle i.c.v. daily (n = 9 rats for control, n = 12 rats for HSD rats treated with vehicle, and n = 16 HSD rats treated with BLZ945), analyzed by one-way ANOVA with Tukey's post hoc test. Data presented as mean \pm SEM; each data point represents one rat; ****p < 0.001, ***p < 0.001, **p < 0.001, and *p < 0.005; ns, not significant.

Microglia-mediated astrocyte pruning contributes to blood pressure increases in HSD

HSD has been shown to increase the firing rate of VP neurons *in vivo*, contributing to elevated blood pressure and hypertension.⁵⁴ To study whether microglia-mediated increases in VP neuron excitation contribute to elevated blood pressure in rats fed HSD, animals were implanted with blood pressure telemetry devices and subjected to either HSD or control diet (Figures 7A and 7B). Consistent with previous studies, rats fed HSD for 7 days displayed elevated mean arterial pressure (MAP) (Figures 7C and 7D). Treating rats with microglial inhibitors PLX3397 (i.p.) or BLZ945 (i.c.v.), but not vehicles, significantly attenuated increases in blood pressure induced by HSD (PLX3397, Figure 7C; BLZ945, Figure 7D). These findings show that microglia-mediated increases in the tonic activation of VP neurons contribute to elevated blood pressure in rats fed HSD.

DISCUSSION

Our study reveals that chronic high-salt intake, which is increasingly present in modern diets, is associated with a local neuroin-flammatory process characterized by an accumulation of reactive microglia around magnocellular VP neurons in the SON and PVN. The microglia engulf and prune local astrocytic processes, impairing their ability to clear glutamate from the synaptic space. This ultimately causes glutamate to activate extrasynaptic NMDARs, contributing to the tonic activation of VP neurons. Furthermore, our findings show that this mechanism

contributes to elevated blood pressure in rats fed HSD and may therefore be an important causal factor in salt-dependent hypertension.

The central role of microglia in remodeling astrocyte networks in HSD

Microglia participate in many critical brain functions, including neurogenesis, synaptogenesis, and myelination, through surveillance, release of soluble factors, and their capacity for phagocytosis during early postnatal development, aging, and disease conditions. 64-67 During development, microglia regulate the abundance of neuronal progenitors by clearing apoptotic or dying newborn neurons, removing non-functional synapses and remodeling synaptic circuits, 48,68,69 and phagocytosing developing oligodendrocytes. 70 In the adult CNS, microglia survey the environment, acting as first responders to acute injury and playing a central role in neurological diseases by clearing dead neurons, debris, and large extracellular aggregates via phagocytosis. These responses typically involve microglia transforming to a reactive state, retracting their processes, forming new motile protrusions, and becoming less ramified and more amoeboid. 64,65,71 Previous studies have demonstrated that astrocyte-microglia communication is important during CNS development, and signaling from astrocytes to microglia promotes synapse engulfment by microglia during circuit maturation.⁷² However, it remains unknown whether microglia can engulf astrocytic material during physiological or pathological plasticity.



Using a classical model where the astrocytic network undergoes substantial structural remodeling, we tested whether microglia can also phagocytose astrocytic material. Our study reveals that hypothalamic microglia can phagocytose and prune astrocytic processes in the adult rat brain. We found that subjecting rats to HSD leads to changes in microglial density and morphology in the SON and PVN (Figure 2). Significant changes in both microglia and astrocytes were detected by day 5 of HSD and became more pronounced by day 7 (Figures S2 and S3). Although non-significant changes in microglial morphology might appear as early as day 2, a marked shift occurs between days 2 and 5, indicating that major alterations take place within this time window. Notably, this gradual transition of microglia to a reactive state parallels a reduction in astrocyte coverage over the same period. Our results suggest that acute application of hypertonic saline to SON brain slices can induce microglial phagocytosis of astrocytic material within minutes (Figure S11). This indicates that, at least ex vivo, microglia can rapidly adopt a phagocytic state, whereas during HSD, this process takes several days. It is conceivable that, as in the case of an acute stimulus, microglial activation in HSD is driven by increased blood osmolality, which gradually rises as animals are exposed to HSD. Further in vivo imaging experiments are needed to clarify the time course of microglial activation, and to determine whether transient increases in blood osmolality can modulate microglial reactivity and induce the engulfment of astrocytic processes under physiological conditions.

HSD-induced changes in microglial density and morphology are specifically localized to areas occupied by VP neuron somata and dendrites in the SON and PVN (Figure 2). Strikingly, microglia located in the adjacent areas, immediately outside the direct proximity of VP neurons, appear to be unaffected, as neither their morphology nor density changes even after 7 days of HSD (Figure S4). Thus, while signals driving changes in microglia remain unknown, it is likely that these signals originate from the neighboring VP neurons. It is conceivable that since magnocellular VP neurons are intrinsically osmosensitive, 73,74 they become more active in response to HSD-induced increases in blood osmolality, 53 and secrete molecules that chemoattract and activate microglia, inducing their transition to a reactive phagocytic state and accumulation around VP neurons.

Specificity of microglial phagocytosis

Our findings suggest that even at rest, SON microglia contain a low number of CD68+ lysosomes, which are much smaller than those found in reactive microglia after 7 days of HSD (Figure 4; Video S1). Some of these small lysosomes contain astrocytic material, suggesting that these microglia might be involved in constitutive astrocytic network remodeling under baseline, non-stimulated conditions. We found that some lysosomes rarely contained also neuronal components, although to a much lesser extent than astrocytic material. Notably, we have not observed lysosomes containing only neuronal material, whereas most lysosomes, particularly in HSD, contained astrocytic material but lacked neuronal markers. Strikingly, HSD led to an approximately 5-fold increase in the number of phagocytic lysosomes, the majority of which contained astrocytic material (Figure 4; Video S2). Despite this increase, there was no corre-

sponding rise in lysosomes containing neuronal material. These findings indicate that HSD induces preferential phagocytosis of astrocytic material, with neuronal material only occasionally co-phagocytosed.

These results are consistent with previous observations reported that while HSD induces reduction in astrocytic coverage, it almost triples the number of synapses and significantly increases the size of neuronal somata and dendrites (neuronal hypertrophy). 9,11,20,32,33,75 Hence, this raises the question of how these reactive microglia can specifically target local astrocytes while mostly avoiding engulfing dense neuronal elements within the SON. It is plausible that HSD also induces changes in astrocytes, potentially triggering the expression of "eat me" tags on the astrocyte surface, marking them for elimination by microglia, or reducing the expression of "don't eat me" signals that would normally protect them from phagocytosis. 76,77

A recent study found that increased endocannabinoid tone during development promotes microglial phagocytosis of astrocytic precursors, influencing newborn astrocyte numbers and neurocircuit maturation in the amygdala. Since magnocellular neurons release endocannabinoids in an activity-dependent manner, HSD-induced increases in magnocellular VP neuron activity may trigger local endocannabinoid release, promoting microglial phagocytosis of astrocytic processes. Moreover, as endocannabinoids can act as chemoattractants, inducing microglial migration, they may mediate microglial accumulation, activation, and engulfment of astrocytic processes around magnocellular VP neurons in HSD.

Many other molecules are upregulated or downregulated in response to HSD, and various candidate signaling molecules or their combinations may be involved in this process. Further experiments are needed to decipher the molecular mechanisms underlying microglial activation in HSD.

Microglia mediate pruning of astrocyte processes

Astrocytes play a central role in sculpting neuronal networks, modulating synaptic transmission, neurotransmitter clearance, and synaptic plasticity.3,4 Thus, structural remodeling of the astrocyte network in HSD can modulate neural activity in multiple ways.5 Previous ultrastructural studies characterized this remarkable structural plasticity of astrocytes and proposed that decreased astrocytic coverage in HSD is mediated by astrocyte "withdrawal" or "retraction." 6,8,9,17,19,20,34 These studies utilized ultrastructural examination with electron microscopy, allowing for the evaluation and quantification of specific details related to neuronal appositions and synaptic number. However, they lack evidence supporting the notion that astrocytes "retract" their processes. We replicated these studies by examining this phenomenon using immunofluorescence, which allows for a more comprehensive analysis of the spatial organization of different cell populations and the quantification of multiple protein components.

Our data reveal that the decrease in astrocyte coverage is associated with a reduction in multiple astrocyte proteins, including GFAP, S100 β , ALDH1L1, GLT1, and vimentin (Figure 1). These changes are associated with a gradual decrease in astrocytic material in the SON and PVN, which can





be quantified and corroborated by immunofluorescence and by analyzing reductions in total SON astrocytic protein levels in HSD-fed rats (Figure S1). Importantly, this reduction is not a result of astrocyte death, but rather a decrease in the density of astrocyte processes, since the total number of SON and PVN astrocytes is not affected by HSD (Figures S2C and S2D).

Traditionally, changes in the expression of certain astrocytic proteins have been linked to astrocyte reactivity. 4,67 For example, genes encoding astrocytic cytoskeletal components, such as the intermediate filament proteins GFAP and vimentin, are upregulated in reactive astrocytes.⁴ Although reactive astrogliosis is a common astrocytic response to brain injury and neuroinflammation, 67 we found no evidence of this response in the SON and PVN following HSD. On the contrary, the levels of these proteins were reduced after HSD. In addition to the astrocytic cytoskeletal proteins, we also evaluated non-structural astrocytic proteins, including the cytosolic enzymes $S100\beta$ and ALDH1L1, as well as the membrane glutamate transporter GLT1. These proteins are not directly linked to reactive astrogliosis, and their levels may either increase or decrease in reactive astrocytes.4 Importantly, all these astrocytic proteins, whether homeostatic or reactive, cytoskeletal, cytosolic, or membrane-associated, were significantly reduced in the SON following HSD. These findings suggest that reduced levels of these proteins reflect the removal of entire cellular fragments, rather than a downregulation of individual astrocytic proteins.

Notably, we demonstrated that these changes are mediated by reactive microglia, which phagocytose astrocytic material (Figure 4; Videos S1 and S2), leading to the reduction in astrocyte coverage. Thus, our data indicate that the decrease in astrocytic coverage in HSD represents microglia-mediated pruning of astrocytes rather than astrocyte retraction.

Microglia-mediated pruning of astrocytes underlies changes in VP neuron activity

While significant changes in astrocyte coverage can affect neuronal excitation through various mechanisms, 55,56,81 we examined the hypothesis that decreased astrocytic coverage causes an impaired synaptic glutamate clearance, leading to glutamate spillover into the extracellular space, thereby activating extrasynaptic glutamate receptors and increasing tonic activation of VP neurons. Our results demonstrate that while in control condition, blocking extrasynaptic NMDARs does not affect the spontaneous firing activity of SON VP neurons, inhibiting these receptors in the SON from HSD-fed rats decreases the firing rate of VP neurons, revealing the presence of a tonic excitatory current in this condition. Furthermore, inhibiting microglia-mediated pruning of astrocytes in HSD restores this effect, suggesting that the dense network of astrocytic processes around VP neurons is essential to prevent the tonic activation of extrasynaptic NMDARs. Our findings suggest that the effectiveness of astrocytes in controlling VP neuron activity and preventing their activation by extrasynaptic NMDARs is mediated by the major glutamate transporter GLT1 (also known as excitatory amino acid transporter 2 or EAAT2). Blocking this transporter increases the spontaneous firing of SON VP neurons in control conditions, mimicking the stimulating effect of HSD on their activity. This also suggests that extrasynaptic NMDARs are normally present on the surface of VP neurons under control conditions but remain inactive due to the efficient removal of extrasynaptic glutamate by astrocytes. Our findings imply that the regulation of VP neuron firing by astrocytes (via the astrocytic transporter GLT1) is controlled by microglia. Blocking microglial activation and proliferation by inhibiting CSF1R-mediated signaling prevents microglia-mediated pruning of astrocytic processes (Figures 3 and S5–S7), diminishes the reduction in GLT1 levels (Figure S9C) and GLT1 function (Figure 5C), and confines the spontaneous firing of VP neurons to control levels (Figure 6J).

Limitations of the pharmacological manipulations of microglia

In this study, we used rats for examining glial plasticity in response to changes in fluid balance. While genetic approaches can be employed to specifically target microglia in mice, for example, by ablating microglia with diphtheria toxin via selective expression of diphtheria toxin receptor in Cx3cr1-Cre or TMEM119-Cre mouse lines, these genetic tools are not available in rats. Targeting microglia in vivo with viruses remains highly challenging, likely due to their macrophage-like ability to eliminate pathogens. Due to the technical limitations in genetically targeting microglia in rats, we used three alternative drugs: PLX3397, PLX5622, and BLZ945, to inhibit CSF1R, a key regulator of microglial activation, proliferation, and survival. 38,39 Previous studies have shown that these drugs can cause partial or complete microglial depletion. 40,41,45,82-84 While these inhibitors are considered specific in targeting CSF1R, 40,41,45 they may have off-target effects. For example, PLX5622 has been shown to affect brain endothelial cholesterol metabolism, in addition to depleting microglia.85

To minimize potential side effects, we used lower drug concentrations. Unlike previous studies that caused microglial ablation with higher concentrations, lower doses in our study did not kill microglia but prevented their accumulation in HSD (Figures 3C, S5C, and S7C). Since systemic administration of the CSF1R inhibitors can also affect peripheral macrophages. 44 we administered BLZ945 directly into the brain, as microglia are the only cell type expressing CSF1R in the CNS. 42,43 Importantly, lower doses of PLX3397 systemically and BLZ945 i.c.v. did not deplete microglia, as we observed no reduction in microglial density in the SON, PVN, or outside these nuclei. Consistent with our interpretation, i.c.v. application of BLZ945 prevented HSD-induced activation of microglia, as it completely reversed the changes in the microglial morphology induced by HSD (Figure 3D). Furthermore, BLZ945 inhibited the HSD-induced accumulation of phagocytic lysosomes in microglia (Figure 4C), confirming that this intervention reverses the transition of microglia to a reactive phagocytic state without affecting microglial survival. These observations support our findings that HSD-mediated activation of microglia leads to microglial pruning of astrocyte processes. Future research should expand on these findings as improved viral and transgenic tools become available, allowing the combination of genetic and pharmacological approaches.

Microglia-driven structural plasticity contributes to saltinduced hypertension

Finally, we showed that interactions between neurons, microglia, and astrocytes determine neuronal activity levels under normal



conditions and underlie functional state-dependent plasticity, facilitating VP neuron firing and systemic VP release, which contribute to salt-dependent hypertension. Inhibiting microglial activation not only prevents structural plasticity of astrocytes and increased excitation of VP neurons, but also significantly reduces HSD-induced increases in blood pressure and attenuates salt-induced hypertension (Figures 7C and 7D).

Since previous studies have demonstrated that increased VP secretion contributes to elevated blood pressure in various models of salt-induced hypertension, ^{53,86,87} we primarily focused on magnocellular VP neurons. However, given that oxytocin is a natriuretic hormone in rats, nearby oxytocin neurons may also be affected by HSD, providing an adaptive mechanism to facilitate sodium excretion and reduce the impact of HSD. Therefore, it is important to investigate whether microglia-mediated pruning of astrocytes also drives changes in oxytocin neuron activity in HSD, or other conditions associated with structural astrocyte plasticity in the magnocellular hypothal-amo-neurohypophysial system.

In summary, our study reveals the capacity of microglia to phagocytose and prune astrocytic processes in the adult brain. These findings uncover a novel mechanism by which microglia can regulate synaptic transmission and neuronal activity via structural remodeling of the astrocytic network. Microglial density and morphology vary between brain regions, 88,89 hence it remains unclear whether the capacity of microglia to remodel astrocytes is unique to the specific hypothalamic region. Future studies should examine whether a similar mechanism can underlie additional forms of structural plasticity in other brain regions under certain physiological or pathological conditions.

RESOURCE AVAILABILITY

Lead contact

Further information and requests for resources and reagents should be directed to the lead contact, Masha Prager-Khoutorsky (masha.prager-khoutorsky@mcgill.ca).

Materials availability

The study did not generate new unique reagents.

Data and code availability

This study did not generate standardized datatypes for public repositories. This paper does not report original code.

All data reported in this paper will be shared by the lead contact upon request.

ACKNOWLEDGMENTS

This work was supported by the Canadian Institutes of Health Research project grants PJT-153009 and 178195 (M.P.-K.) and Azrieli Science grant G-2202-16857 (M.P.-K. and K.Y.C.). M.P.-K. is a recipient of a Heart & Stroke Foundation of Canada National New Investigator Award.

AUTHOR CONTRIBUTIONS

M.P.-K. designed the research program and experiments; N.G., O.M., C.L., C. Q.C., B.L., G.L., J.Y., C.W., and M.P.-K. conducted the experiments; N.G., O. M., C.L., C.Q.C., P.-M.C., B.L., J.Y., C.W., J.F., B.S., S.P.S., M.H., and M.P.-K. analyzed the data; M.M.M. generated and provided Iba1-eGFP rats; M.P.-K.

wrote the manuscript; N.G., K.Y.C., A.K., C.W.B., and M.P.-K. reviewed and edited the manuscript.

DECLARATION OF INTERESTS

The authors declare no competing interests.

STAR*METHODS

Detailed methods are provided in the online version of this paper and include the following:

- KEY RESOURCES TABLE
- EXPERIMENTAL MODEL AND STUDY PARTICIPANT DETAILS
 - o Animals
- METHOD DETAILS
 - o Immunohistochemistry on tissue sections
 - Antibodie
 - Confocal microscopy with AiryScan
 - o Confocal live imaging in acute sections
 - Image analysis and quantification
 - Administration of microglia inhibitors
 - o Acute hypothalamic slice preparations
 - Whole-cell electrophysiology
 - o Blood pressure monitoring
 - Western Blot
- QUANTIFICATION AND STATISTICAL ANALYSIS

SUPPLEMENTAL INFORMATION

Supplemental information can be found online at https://doi.org/10.1016/j.neuron.2025.07.024.

Received: September 8, 2023 Revised: February 18, 2025 Accepted: July 24, 2025

REFERENCES

- Theodosis, D.T., Poulain, D.A., and Oliet, S.H.R. (2008). Activity-dependent structural and functional plasticity of astrocyte-neuron interactions. Physiol. Rev. 88, 983–1008. https://doi.org/10.1152/physrev.00036.2007.
- Brandebura, A.N., Paumier, A., Onur, T.S., and Allen, N.J. (2023). Astrocyte contribution to dysfunction, risk and progression in neurode-generative disorders. Nat. Rev. Neurosci. 24, 23–39. https://doi.org/10.1038/s41583-022-00641-1.
- Dallérac, G., Zapata, J., and Rouach, N. (2018). Versatile control of synaptic circuits by astrocytes: where, when and how? Nat. Rev. Neurosci. 19, 729–743. https://doi.org/10.1038/s41583-018-0080-6.
- Verkhratsky, A., and Nedergaard, M. (2018). Physiology of Astroglia. Physiol. Rev. 98, 239–389. https://doi.org/10.1152/physrev.00042.2016.
- Lawal, O., Ulloa Severino, F.P., and Eroglu, C. (2022). The role of astrocyte structural plasticity in regulating neural circuit function and behavior. Glia 70, 1467–1483. https://doi.org/10.1002/glia.24191.
- Clasadonte, J., and Prevot, V. (2018). The special relationship: glia-neuron interactions in the neuroendocrine hypothalamus. Nat. Rev. Endocrinol. 14, 25–44. https://doi.org/10.1038/nrendo.2017.124.
- Oliet, S.H., and Piet, R. (2004). Anatomical remodelling of the supraoptic nucleus: changes in synaptic and extrasynaptic transmission.
 J. Neuroendocrinol. 16, 303–307. https://doi.org/10.1111/j.0953-8194. 2004.01159.x.
- Salm, A.K. (2000). Mechanisms of glial retraction in the hypothalamoneurohypophysial system of the rat. Exp. Physiol. 85, 1978–202S. https://doi.org/10.1111/j.1469-445x.2000.tb00024.x.





- Hatton, G.I. (1997). Function-related plasticity in hypothalamus. Annu. Rev. Neurosci. 20, 375–397. https://doi.org/10.1146/annurev.neuro.20. 1.375.
- Theodosis, D.T., and Poulain, D.A. (1999). Contribution of astrocytes to activity-dependent structural plasticity in the adult brain. Adv. Exp. Med. Biol. 468, 175–182. https://doi.org/10.1007/978-1-4615-4685-6_14.
- Chapman, D.B., Theodosis, D.T., Montagnese, C., Poulain, D.A., and Morris, J.F. (1986). Osmotic stimulation causes structural plasticity of neurone-glia relationships of the oxytocin but not vasopressin secreting neurones in the hypothalamic supraoptic nucleus. Neuroscience 17, 679–686. https://doi.org/10.1016/0306-4522(86)90039-4.
- Theodosis, D.T., Chapman, D.B., Montagnese, C., Poulain, D.A., and Morris, J.F. (1986). Structural plasticity in the hypothalamic supraoptic nucleus at lactation affects oxytocin-, but not vasopressin-secreting neurones. Neuroscience 17, 661–678. https://doi.org/10.1016/0306-4522(86) 90038-2.
- Theodosis, D.T., and Poulain, D.A. (1984). Evidence for structural plasticity in the supraoptic nucleus of the rat hypothalamus in relation to gestation and lactation. Neuroscience 11, 183–193. https://doi.org/10.1016/0306-4522(84)90222-7.
- Theodosis, D.T., Montagnese, C., Rodriguez, F., Vincent, J.D., and Poulain, D.A. (1986). Oxytocin induces morphological plasticity in the adult hypothalamo-neurohypophysial system. Nature 322, 738–740. https://doi. org/10.1038/322738a0.
- Theodosis, D.T., Poulain, D.A., and Vincent, J.D. (1981). Possible morphological bases for synchronisation of neuronal firing in the rat supraoptic nucleus during lactation. Neuroscience 6, 919–929. https://doi.org/10.1016/0306-4522(81)90173-1.
- Choe, K.Y., Olson, J.E., and Bourque, C.W. (2012). Taurine release by astrocytes modulates osmosensitive glycine receptor tone and excitability in the adult supraoptic nucleus. J. Neurosci. 32, 12518–12527. https://doi.org/10.1523/JNEUROSCI.1380-12.2012.
- Hatton, G.I. (2004). Dynamic neuronal-glial interactions: an overview 20 years later. Peptides 25, 403–411. https://doi.org/10.1016/j.peptides. 2003.12.001.
- Tweedle, C.D., and Hatton, G.I. (1976). Ultrastructural comparisons of neurons of supraoptic and circularis nuclei in normal and dehydrated rats. Brain Res. Bull. 1, 103–121. https://doi.org/10.1016/0361-9230(76) 90054-x.
- Tweedle, C.D., and Hatton, G.I. (1977). Ultrastructural changes in rat hypothalamic neurosecretory cells and their associated glia during minimal dehydration and rehydration. Cell Tissue Res. 181, 59–72. https://doi.org/10.1007/BF00222774.
- Theodosis, D.T., and Poulain, D.A. (1993). Activity-dependent neuronalglial and synaptic plasticity in the adult mammalian hypothalamus. Neuroscience 57, 501–535. https://doi.org/10.1016/0306-4522(93) 90002-w.
- Johnson, R.F., Beltz, T.G., Johnson, A.K., and Thunhorst, R.L. (2015).
 Effects of fludrocortisone on water and sodium intake of C57BL/6 mice.
 Am. J. Physiol. Regul. Integr. Comp. Physiol. 309, R247–R254. https://doi.org/10.1152/ajpregu.00033.2015.
- Yang, B., and Bankir, L. (2005). Urea and urine concentrating ability: new insights from studies in mice. Am. J. Physiol. Ren. Physiol. 288, F881– F896. https://doi.org/10.1152/ajprenal.00367.2004.
- Bankir, L., and de Rouffignac, C. (1985). Urinary concentrating ability: insights from comparative anatomy. Am. J. Physiol. 249, R643–R666. https://doi.org/10.1152/ajpregu.1985.249.6.R643.
- Beuchat, C.A. (1990). Body size, medullary thickness, and urine concentrating ability in mammals. Am. J. Physiol. 258, R298–R308. https://doi.org/10.1152/ajpregu.1990.258.2.R298.
- Schmidt-Nielsen, K., Schmidt-Nielsen, B., and Schneiderman, H. (1948).
 Salt excretion in desert mammals. Am. J. Physiol. 154, 163–166. https://doi.org/10.1152/ajplegacy.1948.154.1.163.

- Schmidt-Nielsen, K., and Schmidt-Nielsen, B. (1952). Water metabolism of desert mammals 1. Physiol. Rev. 32, 135–166. https://doi.org/10.1152/ physrev.1952.32.2.135.
- Marra, N.J., Romero, A., and DeWoody, J.A. (2014). Natural selection and the genetic basis of osmoregulation in heteromyid rodents as revealed by RNA-seq. Mol. Ecol. 23, 2699–2711. https://doi.org/10.1111/mec.12764.
- Cassis, L.A., Huang, J., Gong, M.C., and Daugherty, A. (2004). Role of metabolism and receptor responsiveness in the attenuated responses to Angiotensin II in mice compared to rats. Regul. Pept. 117, 107–116. https://doi.org/10.1016/j.regpep.2003.09.008.
- Nomura, K., Hiyama, T.Y., Sakuta, H., Matsuda, T., Lin, C.H., Kobayashi, K., Kobayashi, K., Kuwaki, T., Takahashi, K., Matsui, S., et al. (2019). [Na+] Increases in Body Fluids Sensed by Central Nax Induce Sympathetically Mediated Blood Pressure Elevations via H+-Dependent Activation of ASIC1a. Neuron 101, 60–75.e6. https://doi.org/10.1016/j.neuron.2018.11.017.
- Hu, J., Luo, H., Wang, J., Tang, W., Lu, J., Wu, S., Xiong, Z., Yang, G., Chen, Z., Lan, T., et al. (2017). Enteric dysbiosis-linked gut barrier disruption triggers early renal injury induced by chronic high salt feeding in mice. Exp. Mol. Med. 49, e370. https://doi.org/10.1038/emm.2017.122.
- Zhou, X., Chen, K., Lei, H., and Sun, Z. (2015). Klotho gene deficiency causes salt-sensitive hypertension via monocyte chemotactic protein-1/ CC chemokine receptor 2-mediated inflammation. J. Am. Soc. Nephrol. 26, 121–132. https://doi.org/10.1681/ASN.2013101033.
- Tweedle, C.D., and Hatton, G.I. (1984). Synapse formation and disappearance in adult rat supraoptic nucleus during different hydration states. Brain Res. 309, 373–376. https://doi.org/10.1016/0006-8993(84)90607-3.
- Perlmutter, L.S., Tweedle, C.D., and Hatton, G.I. (1985). Neuronal/glial plasticity in the supraoptic dendritic zone in response to acute and chronic dehydration. Brain Res. 361, 225–232. https://doi.org/10.1016/0006-8993 (85)91293-4
- Tasker, J.G., Oliet, S.H., Bains, J.S., Brown, C.H., and Stern, J.E. (2012).
 Glial regulation of neuronal function: from synapse to systems physiology.
 J. Neuroendocrinol. 24, 566–576. https://doi.org/10.1111/j.1365-2826.
 2011.02259.x.
- Wu, Y., Dissing-Olesen, L., MacVicar, B.A., and Stevens, B. (2015).
 Microglia: Dynamic Mediators of Synapse Development and Plasticity.
 Trends Immunol. 36, 605–613. https://doi.org/10.1016/j.it.2015.08.008.
- Hong, S., Dissing-Olesen, L., and Stevens, B. (2016). New insights on the role of microglia in synaptic pruning in health and disease. Curr. Opin. Neurobiol. 36, 128–134. https://doi.org/10.1016/j.conb.2015.12.004.
- Paolicelli, R.C., Sierra, A., Stevens, B., Tremblay, M.E., Aguzzi, A., Ajami, B., Amit, I., Audinat, E., Bechmann, I., Bennett, M., et al. (2022). Microglia states and nomenclature: A field at its crossroads. Neuron 110, 3458– 3483. https://doi.org/10.1016/j.neuron.2022.10.020.
- Rice, R.A., Spangenberg, E.E., Yamate-Morgan, H., Lee, R.J., Arora, R.P. S., Hernandez, M.X., Tenner, A.J., West, B.L., and Green, K.N. (2015).
 Elimination of Microglia Improves Functional Outcomes Following Extensive Neuronal Loss in the Hippocampus. J. Neurosci. 35, 9977–9989. https://doi.org/10.1523/JNEUROSCI.0336-15.2015.
- Yang, X., Ren, H., Wood, K., Li, M., Qiu, S., Shi, F.D., Ma, C., and Liu, Q. (2018). Depletion of microglia augments the dopaminergic neurotoxicity of MPTP. FASEB J. 32, 3336–3345. https://doi.org/10.1096/fj.201700833RR.
- Guenoun, D., Blaise, N., Sellam, A., Roupret-Serzec, J., Jacquens, A., Steenwinckel, J.V., Gressens, P., and Bokobza, C. (2025). Microglial Depletion, a New Tool in Neuroinflammatory Disorders: Comparison of Pharmacological Inhibitors of the CSF-1R. Glia 73, 686–700. https://doi. org/10.1002/glia.24664.
- Dagher, N.N., Najafi, A.R., Kayala, K.M.N., Elmore, M.R.P., White, T.E., Medeiros, R., West, B.L., and Green, K.N. (2015). Colony-stimulating factor 1 receptor inhibition prevents microglial plaque association and



- improves cognition in 3xTg-AD mice. J. Neuroinflammation 12, 139. https://doi.org/10.1186/s12974-015-0366-9.
- Erblich, B., Zhu, L., Etgen, A.M., Dobrenis, K., and Pollard, J.W. (2011).
 Absence of colony stimulation factor-1 receptor results in loss of microglia, disrupted brain development and olfactory deficits. PLoS One 6, e26317. https://doi.org/10.1371/journal.pone.0026317.
- Nandi, S., Gokhan, S., Dai, X.M., Wei, S., Enikolopov, G., Lin, H., Mehler, M.F., and Stanley, E.R. (2012). The CSF-1 receptor ligands IL-34 and CSF-1 exhibit distinct developmental brain expression patterns and regulate neural progenitor cell maintenance and maturation. Dev. Biol. 367, 100–113. https://doi.org/10.1016/j.ydbio.2012.03.026.
- Lei, F., Cui, N., Zhou, C., Chodosh, J., Vavvas, D.G., and Paschalis, E.I. (2020). CSF1R inhibition by a small-molecule inhibitor is not microglia specific; affecting hematopoiesis and the function of macrophages. Proc. Natl. Acad. Sci. USA 117, 23336–23338. https://doi.org/10.1073/pnas.1922788117.
- Luczak-Sobotkowska, Z.M., Rosa, P., Lopez, M.B., Ochocka, N., Kiryk, A., Lenkiewicz, A.M., Furhmann, M., Jankowski, A., and Kaminska, B. (2024). Tracking changes in functionality and morphology of repopulated microglia in young and old mice. J. Neuroinflammation 21, 248. https:// doi.org/10.1186/s12974-024-03242-0.
- Hong, S., and Stevens, B. (2016). Microglia: Phagocytosing to Clear, Sculpt, and Eliminate. Dev. Cell 38, 126–128. https://doi.org/10.1016/j. devcel.2016.07.006.
- Mendiola, A.S., and Cardona, A.E. (2018). The IL-1beta phenomena in neuroinflammatory diseases. J. Neural Transm. (Vienna) 125, 781–795. https://doi.org/10.1007/s00702-017-1732-9.
- Schafer, D.P., Lehrman, E.K., Kautzman, A.G., Koyama, R., Mardinly, A.R., Yamasaki, R., Ransohoff, R.M., Greenberg, M.E., Barres, B.A., and Stevens, B. (2012). Microglia sculpt postnatal neural circuits in an activity and complement-dependent manner. Neuron 74, 691–705. https://doi. org/10.1016/j.neuron.2012.03.026.
- Tanaka, Y., Matsuwaki, T., Yamanouchi, K., and Nishihara, M. (2013). Increased lysosomal biogenesis in activated microglia and exacerbated neuronal damage after traumatic brain injury in progranulin-deficient mice. Neuroscience 250, 8–19. https://doi.org/10.1016/j.neuroscience. 2013.06.049.
- Langle, S.L., Poulain, D.A., and Theodosis, D.T. (2003). Induction of rapid, activity-dependent neuronal-glial remodelling in the adult rat hypothalamus in vitro. Eur. J. Neurosci. 18, 206–214. https://doi.org/10.1046/j. 1460-9568.2003.02741.x.
- 51. Baudon, A., Grelot, V., Althammer, F., Wang, K.-Y., Denis, C., Ali, S.A., Yan, Y., Castillo-Diaz, F., Piacentini, F., Creusot, E.C., et al. (2024). Oxytocin Gα_i signaling-induced amygdala astrocytes processes retraction shapes behavioral stress response. Preprint at bioRxiv. https://doi.org/10.1101/2024.10.07.617014.
- VanRyzin, J.W., Arambula, S.E., Ashton, S.E., Blanchard, A.C., Burzinski, M.D., Davis, K.T., Edwards, S., Graham, E.L., Holley, A., Kight, K.E., et al. (2021). Generation of an Iba1-EGFP Transgenic Rat for the Study of Microglia in an Outbred Rodent Strain. eNeuro 8, ENEURO.0026-21.2021. https://doi.org/10.1523/ENEURO.0026-21.2021.
- Levi, D.I., Wyrosdic, J.C., Hicks, A.I., Andrade, M.A., Toney, G.M., Prager-Khoutorsky, M., and Bourque, C.W. (2021). High dietary salt amplifies osmoresponsiveness in vasopressin-releasing neurons. Cell Rep. 34, 108866. https://doi.org/10.1016/j.celrep.2021.108866.
- 54. Choe, K.Y., Han, S.Y., Gaub, P., Shell, B., Voisin, D.L., Knapp, B.A., Barker, P.A., Brown, C.H., Cunningham, J.T., and Bourque, C.W. (2015). High salt intake increases blood pressure via BDNF-mediated downregulation of KCC2 and impaired baroreflex inhibition of vasopressin neurons. Neuron 85, 549–560. https://doi.org/10.1016/j.neuron.2014.12.048.
- Oliet, S.H., Piet, R., and Poulain, D.A. (2001). Control of glutamate clearance and synaptic efficacy by glial coverage of neurons. Science 292, 923–926. https://doi.org/10.1126/science.1059162.

- Panatier, A., Theodosis, D.T., Mothet, J.P., Touquet, B., Pollegioni, L., Poulain, D.A., and Oliet, S.H.R. (2006). Glia-derived D-serine controls NMDA receptor activity and synaptic memory. Cell 125, 775–784. https://doi.org/10.1016/j.cell.2006.02.051.
- Papouin, T., and Oliet, S.H.R. (2014). Organization, control and function of extrasynaptic NMDA receptors. Philos. Trans. R. Soc. Lond. B Biol. Sci. 369, 20130601. https://doi.org/10.1098/rstb.2013.0601.
- Fleming, T.M., Scott, V., Naskar, K., Joe, N., Brown, C.H., and Stern, J.E. (2011). State-dependent changes in astrocyte regulation of extrasynaptic NMDA receptor signalling in neurosecretory neurons. J. Physiol. 589, 3929–3941. https://doi.org/10.1113/jphysiol.2011.207340.
- Joe, N., Scott, V., and Brown, C.H. (2014). Glial regulation of extrasynaptic NMDA receptor-mediated excitation of supraoptic nucleus neurones during dehydration. J. Neuroendocrinol. 26, 35–42. https://doi.org/10.1111/ jne.12121.
- Ueta, Y., Fujihara, H., Serino, R., Dayanithi, G., Ozawa, H., Matsuda, K., Kawata, M., Yamada, J., Ueno, S., Fukuda, A., et al. (2005). Transgenic expression of enhanced green fluorescent protein enables direct visualization for physiological studies of vasopressin neurons and isolated nerve terminals of the rat. Endocrinology 146, 406–413. https://doi.org/10. 1210/en.2004-0830.
- Williams, K. (1993). Ifenprodil discriminates subtypes of the N-methyl-D-aspartate receptor: selectivity and mechanisms at recombinant heteromeric receptors. Mol. Pharmacol. 44, 851–859. https://doi.org/10.1016/S0026-895X(25)13275-6.
- Tovar, K.R., and Westbrook, G.L. (1999). The incorporation of NMDA receptors with a distinct subunit composition at nascent hippocampal synapses in vitro. J. Neurosci. 19, 4180–4188. https://doi.org/10.1523/JNEUROSCI.19-10-04180.1999.
- Li, B., Chen, N., Luo, T., Otsu, Y., Murphy, T.H., and Raymond, L.A. (2002).
 Differential regulation of synaptic and extra-synaptic NMDA receptors.
 Nat. Neurosci. 5, 833–834. https://doi.org/10.1038/nn912.
- Gao, C., Jiang, J., Tan, Y., and Chen, S. (2023). Microglia in neurodegenerative diseases: mechanism and potential therapeutic targets. Signal Transduct. Target. Ther. 8, 359. https://doi.org/10.1038/s41392-023-01588-0
- Tremblay, M.È., and Verkhratsky, A. (2024). General Pathophysiology of Microglia. Adv. Neurobiol. 37, 3–14. https://doi.org/10.1007/978-3-031-55529-9_1.
- Wake, H., Moorhouse, A.J., Miyamoto, A., and Nabekura, J. (2013). Microglia: actively surveying and shaping neuronal circuit structure and function. Trends Neurosci. 36, 209–217. https://doi.org/10.1016/j.tins. 2012.11.007.
- Escartin, C., Galea, E., Lakatos, A., O'Callaghan, J.P., Petzold, G.C., Serrano-Pozo, A., Steinhäuser, C., Volterra, A., Carmignoto, G., Agarwal, A., et al. (2021). Reactive astrocyte nomenclature, definitions, and future directions. Nat. Neurosci. 24, 312–325. https://doi.org/10. 1038/s41593-020-00783-4.
- Tremblay, M.E., Lowery, R.L., and Majewska, A.K. (2010). Microglial interactions with synapses are modulated by visual experience. PLoS Biol. 8, e1000527. https://doi.org/10.1371/journal.pbio.1000527.
- Stevens, B., Allen, N.J., Vazquez, L.E., Howell, G.R., Christopherson, K.S., Nouri, N., Micheva, K.D., Mehalow, A.K., Huberman, A.D., Stafford, B., et al. (2007). The classical complement cascade mediates CNS synapse elimination. Cell 131, 1164–1178. https://doi.org/10.1016/j.cell.2007. 10.036.
- Li, Q., Cheng, Z., Zhou, L., Darmanis, S., Neff, N.F., Okamoto, J., Gulati, G., Bennett, M.L., Sun, L.O., Clarke, L.E., et al. (2019). Developmental Heterogeneity of Microglia and Brain Myeloid Cells Revealed by Deep Single-Cell RNA Sequencing. Neuron 101, 207–223.e10. https://doi.org/ 10.1016/j.neuron.2018.12.006.
- Tremblay, M.È. (2021). Microglial functional alteration and increased diversity in the challenged brain: Insights into novel targets for intervention.





- Brain Behav. Immun Health 16, 100301. https://doi.org/10.1016/j.bbih. 2021.100301.
- Vainchtein, I.D., Chin, G., Cho, F.S., Kelley, K.W., Miller, J.G., Chien, E.C., Liddelow, S.A., Nguyen, P.T., Nakao-Inoue, H., Dorman, L.C., et al. (2018). Astrocyte-derived interleukin-33 promotes microglial synapse engulfment and neural circuit development. Science 359, 1269–1273. https://doi.org/ 10.1126/science.aal3589.
- Oliet, S.H., and Bourque, C.W. (1993). Mechanosensitive channels transduce osmosensitivity in supraoptic neurons. Nature 364, 341–343. https://doi.org/10.1038/364341a0.
- Bourque, C.W. (2008). Central mechanisms of osmosensation and systemic osmoregulation. Nat. Rev. Neurosci. 9, 519–531. https://doi.org/10.1038/nrn2400.
- Modney, B.K., and Hatton, G.I. (1989). Multiple synapse formation: a possible compensatory mechanism for increased cell size in rat supraoptic nucleus. J. Neuroendocrinol. 1, 21–27. https://doi.org/10.1111/j.1365-2826.1989.tb00072.x.
- Lehrman, E.K., Wilton, D.K., Litvina, E.Y., Welsh, C.A., Chang, S.T., Frouin, A., Walker, A.J., Heller, M.D., Umemori, H., Chen, C., et al. (2018). CD47 Protects Synapses from Excess Microglia-Mediated Pruning during Development. Neuron 100, 120–134.e6. https://doi.org/10.1016/j. neuron.2018.09.017.
- Wilton, D.K., Dissing-Olesen, L., and Stevens, B. (2019). Neuron-Glia Signaling in Synapse Elimination. Annu. Rev. Neurosci. 42, 107–127. https://doi.org/10.1146/annurev-neuro-070918-050306.
- VanRyzin, J.W., Marquardt, A.E., Argue, K.J., Vecchiarelli, H.A., Ashton, S. E., Arambula, S.E., Hill, M.N., and McCarthy, M.M. (2019). Microglial Phagocytosis of Newborn Cells Is Induced by Endocannabinoids and Sculpts Sex Differences in Juvenile Rat Social Play. Neuron 102, 435–449.e6. https://doi.org/10.1016/j.neuron.2019.02.006.
- Di, S., Boudaba, C., Popescu, I.R., Weng, F.J., Harris, C., Marcheselli, V. L., Bazan, N.G., and Tasker, J.G. (2005). Activity-dependent release and actions of endocannabinoids in the rat hypothalamic supraoptic nucleus. J. Physiol. 569, 751–760. https://doi.org/10.1113/jphysiol.2005.097477.
- Walter, L., Franklin, A., Witting, A., Wade, C., Xie, Y., Kunos, G., Mackie, K., and Stella, N. (2003). Nonpsychotropic cannabinoid receptors regulate microglial cell migration. J. Neurosci. 23, 1398–1405. https://doi.org/10. 1523/JNEUROSCI.23-04-01398.2003.
- Piet, R., Vargová, L., Syková, E., Poulain, D.A., and Oliet, S.H.R. (2004).
 Physiological contribution of the astrocytic environment of neurons to intersynaptic crosstalk. Proc. Natl. Acad. Sci. USA 101, 2151–2155. https://doi.org/10.1073/pnas.0308408100.
- Merry, T.L., Brooks, A.E.S., Masson, S.W., Adams, S.E., Jaiswal, J.K., Jamieson, S.M.F., and Shepherd, P.R. (2020). The CSF1 receptor inhibitor pexidartinib (PLX3397) reduces tissue macrophage levels without affecting glucose homeostasis in mice. Int. J. Obes. (Lond.) 44, 245–253. https://doi.org/10.1038/s41366-019-0355-7.
- Spangenberg, E., Severson, P.L., Hohsfield, L.A., Crapser, J., Zhang, J., Burton, E.A., Zhang, Y., Spevak, W., Lin, J., Phan, N.Y., et al. (2019). Sustained microglial depletion with CSF1R inhibitor impairs parenchymal plaque development in an Alzheimer's disease model. Nat. Commun. 10, 3758. https://doi.org/10.1038/s41467-019-11674-z.
- 84. Beckmann, N., Giorgetti, E., Neuhaus, A., Zurbruegg, S., Accart, N., Smith, P., Perdoux, J., Perrot, L., Nash, M., Desrayaud, S., et al. (2018). Brain region-specific enhancement of remyelination and prevention of demyelin-

- ation by the CSF1R kinase inhibitor BLZ945. Acta Neuropathol. Commun. 6, 9. https://doi.org/10.1186/s40478-018-0510-8.
- Profaci, C.P., Harvey, S.S., Bajc, K., Zhang, T.Z., Jeffrey, D.A., Zhang, A. Z., Nemec, K.M., Davtyan, H., O'Brien, C.A., McKinsey, G.L., et al. (2024). Microglia are not necessary for maintenance of blood-brain barrier properties in health, but PLX5622 alters brain endothelial cholesterol metabolism. Neuron 112, 2910–2921.e7. https://doi.org/10.1016/j.neuron. 2024.07.015.
- Choe, K.Y., Trudel, E., and Bourque, C.W. (2016). Effects of Salt Loading on the Regulation of Rat Hypothalamic Magnocellular Neurosecretory Cells by Ionotropic GABA and Glycine Receptors. J. Neuroendocrinol. 28. https://doi.org/10.1111/jne.12372.
- Kim, Y.B., Kim, Y.S., Kim, W.B., Shen, F.Y., Lee, S.W., Chung, H.J., Kim, J. S., Han, H.C., Colwell, C.S., and Kim, Y.I. (2013). GABAergic excitation of vasopressin neurons: possible mechanism underlying sodium-dependent hypertension. Circ. Res. 113, 1296–1307. https://doi.org/10.1161/CIRCRESAHA.113.301814.
- Lawson, L.J., Perry, V.H., Dri, P., and Gordon, S. (1990). Heterogeneity in the distribution and morphology of microglia in the normal adult mouse brain. Neuroscience 39, 151–170. https://doi.org/10.1016/0306-4522(90) 90229-w.
- Mazeraud, A., Pascal, Q., Verdonk, F., Heming, N., Chrétien, F., and Sharshar, T. (2016). Neuroanatomy and Physiology of Brain Dysfunction in Sepsis. Clin. Chest Med. 37, 333–345. https://doi.org/10.1016/j.ccm. 2016.01.013.
- Ben-Barak, Y., Russell, J.T., Whitnall, M.H., Ozato, K., and Gainer, H. (1985). Neurophysin in the hypothalamo-neurohypophysial system. I. Production and characterization of monoclonal antibodies. J. Neurosci. 5, 81–97. https://doi.org/10.1523/JNEUROSCI.05-01-00081.1985.
- Hicks, A.I., Barad, Z., Sobrero, A., Lean, G., Jacob-Tomas, S., Yang, J., Choe, K.Y., and Prager-Khoutorsky, M. (2020). Effects of salt loading on the organisation of microtubules in rat magnocellular vasopressin neurones. J. Neuroendocrinol. 32, e12817. https://doi.org/10.1111/jne.12817.
- Barad, Z., Jacob-Tomas, S., Sobrero, A., Lean, G., Hicks, A.I., Yang, J., Choe, K.Y., and Prager-Khoutorsky, M. (2020). Unique Organization of Actin Cytoskeleton in Magnocellular Vasopressin Neurons in Normal Conditions and in Response to Salt-Loading. eNeuro 7, ENEURO.0351-19.2020. https://doi.org/10.1523/ENEURO.0351-19.2020.
- Miyata, S., and Hatton, G.I. (2002). Activity-related, dynamic neuron-glial interactions in the hypothalamo-neurohypophysial system. Microsc. Res. Tech. 56, 143–157. https://doi.org/10.1002/jemt.10012.
- Alonso, G., Galibert, E., Duvoid-Guillou, A., and Vincent, A. (2005).
 Hyperosmotic stimulus induces reversible angiogenesis within the hypothalamic magnocellular nuclei of the adult rat: a potential role for neuronal vascular endothelial growth factor. BMC Neurosci. 6, 20. https://doi.org/10.1186/1471-2202-6-20.
- Trudel, E., and Bourque, C.W. (2010). Central clock excites vasopressin neurons by waking osmosensory afferents during late sleep. Nat. Neurosci. 13, 467–474. https://doi.org/10.1038/nn.2503.
- Althammer, F., Ferreira-Neto, H.C., Rubaharan, M., Roy, R.K., Patel, A.A., Murphy, A., Cox, D.N., and Stern, J.E. (2020). Three-dimensional morphometric analysis reveals time-dependent structural changes in microglia and astrocytes in the central amygdala and hypothalamic paraventricular nucleus of heart failure rats. J. Neuroinflammation 17, 221. https://doi.org/ 10.1186/s12974-020-01892-4.

Neuron Article



STAR*METHODS

KEY RESOURCES TABLE

REAGENT or RESOURCE	SOURCE	IDENTIFIER
ntibodies		
asopressin	SYSY	Cat# 403-004; RRID: AB_2725758
oxytocin	Provided by Dr. Hal Gainer ⁹⁰	Cat# PS-38; RRID: AB_2315026
iFAP	Abcam	Cat# ab4674; RRID:AB_322219
:100β	Abcam	Cat# ab52642; RRID:AB_882426
LDH1L1	Proteintech	Cat# 17390-1-AP; RRID:AB_2878401
iLT1	Abcam	Cat# ab106289; RRID:AB_10866196
imentin	DSHB	Cat# 40ECs; RRID:AB_528504
pa1	Wako	Cat# 019-19741; RRID:AB_839504
pa1	SYSY	Cat# 234-308; RRID:AB_2924932
MEM119	SYSY	Cat# 400-203; RRID:AB_2832239
D68	Bio-Rad	Cat# MCA341GA; RRID:AB_556872
euN	Sigma-Aldrich	Cat# ABN90; RRID:AB_11205592
-actin	Sigma-Aldrich	Cat# a5441; RRID:AB_476744
FAP	Sigma-Aldrich	Cat# G4546; RRID:AB_1840895
ioat anti -mouse Alexa Fluor 405	Thermo Fisher Scientific	Cat#A-31553; RRID: AB_221604
ioat anti -mouse Alexa Fluor 488	Thermo Fisher Scientific	Cat# A-11029; RRID:AB_2534088
ioat anti -mouse Alexa Fluor 647	Thermo Fisher Scientific	Cat# A-21235; RRID:AB_2535804
oat anti -mouse Alexa Fluor 488 (IgM)	Thermo Fisher Scientific	Cat# A-10680; RRID:AB_2534062
oat anti -rabbit Alexa Fluor 488	Thermo Fisher Scientific	Cat# A-11034; RRID:AB_ 2576217
oat anti -rabbit Alexa Fluor 568	Thermo Fisher Scientific	Cat# A-11036; RRID:AB_10563566
oat anti -rabbit Alexa Fluor 647	Thermo Fisher Scientific	Cat# A-21245; RRID:AB_2535813
oat anti -guinea pig Alexa Fluor 568	Thermo Fisher Scientific	Cat# A-11075; RRID:AB_2534119
oat anti -guinea pig Alexa Fluor 647	Thermo Fisher Scientific	Cat# A-21450; RRID: AB_2535867
oat anti -chicken Alexa Fluor 488	Thermo Fisher Scientific	Cat# A-11039; RRID:AB_2534096
oat anti -chicken Alexa Fluor 568	Thermo Fisher Scientific	Cat# A-11041; RRID:AB_2534098
oat anti -chicken Alexa Fluor 647	Thermo Fisher Scientific	Cat# A-32933; RRID:AB_2762845
oat anti-mouse HRP	Thermo Fisher Scientific	Cat# 31430; RRID:AB_228307
oat anti-rabbit HRP	Thermo Fisher Scientific	Cat# 31460; RRID:AB_228341
acterial and virus strains		
AV6-gfaABC1DtdTomato	Canadian Neurophotonics Platform Viral Vector Core Facility	RRID:SCR_016477
hemicals, peptides, and recombinant proteins		
LX5622	MedChemExpress	Cat# HY-114153; CAS# 1303420-67-8
LX3397 (Pexidartinib)	MedChemExpress	Cat# HY-116749; CAS# 1029044-16-3
LZ945 (Sotuletinib)	MedChemExpress	Cat# HY-12768; CAS# 953769-46-5
ihydrokainate (DHK)	Millipore Sigma	Cat# D1064; CAS#52497-36-6
enprodil	Millipore Sigma	Cat# I2892; CAS#23210-58-4
R)-amino-5-phosphonovaleric acid (AP-5)	Sigma Aldrich	Cat# A8054; CAS# 76326-31-3
ynurenic acid (KYN)	Millipore Sigma	Cat# K3375; CAS#492-27-3
etradotoxin (TTX)	Alomone labs	Cat# T-500; CAS#4368-28-9
xperimental models: Organisms/strains		
at: Wistar	Charles River	Cat# T-273; RRID: 2308816
at: Wistar AVP-eGFP	Ueta et al.60	N/A

(Continued on next page)





Continued		
REAGENT or RESOURCE	SOURCE	IDENTIFIER
Rat: Sprague Dawley Iba1-eGFP	VanRyzin et al. ⁵²	N/A
Software and algorithms		
AcqKnowledge BIOPAC	BIOPAC	RRID: SCR_014279
ChemiDoc Imaging System	BioRad	RRID: SCR_014210
GraphPad Prism 9.1.0	Prism	RRID:SCR_002798
pCLAMP 11.0	Molecular Devices	RRID: SCR_011323
IMARIS software (Version 10.1.1)	Oxford Instruments	RRID:SCR_007370
Zeiss LSM 880 with Airyscan Confocal Laser Scanning Microscope	Zeiss	RRID:SCR_020925
Zeiss Zen Blue	Zeiss	RRID: SCR_013672
Zeiss Zen Black	Zeiss	RRID: SCR_018163
FIJI	NIH	RRID: SCR_002285
PhenoMaster	TSE Systems	N/A
Stellar Telemetry	TSE Systems	N/A

EXPERIMENTAL MODEL AND STUDY PARTICIPANT DETAILS

Animals

Male and female adult Wistar rats (300-400 g; Charles River Laboratories Inc., Saint-Constant, Quebec) were used throughout this study, unless indicated. Rats were treated in strict accordance with the guidelines outlined by the Canadian Council on Animal Care (http://www.ccac.ca/) and experiments adhered to protocols #AUP7948 approved by the Facility Animal Care Committee of McGill University. All animals were kept in a climate-controlled room under a standard 12/12h light/dark cycle, habituated to individual housing in behavioral cages for 10 days before experimental procedures (PhenoMaster, TSE Systems). Food and water were provided *ad libitum*. HSD-treated rats were provided with 2% NaCl solution as drinking fluid instead of water for 2-7 days as described previously. ^{53,54,91,92} Electrophysiological experiments were performed on in-house bred transgenic Wistar rats (8-12 weeks old) expressing enhanced green fluorescent protein (eGFP) under the control of the Avp gene promoter. ⁶⁰ Male and female rats were analyzed separately, and since no differences were detected, sexes were pooled and analysed together. In all experiments, animals were randomly assigned to different groups. The experimenter was blinded to the experimental condition in all studies.

METHOD DETAILS

Immunohistochemistry on tissue sections

Rats were transcardially perfused with 10 ml of phosphate-buffered saline (PBS) and then with 250 ml of PBS containing 4% paraformaldehyde and 0.25% glutaraldehyde, pH adjusted to 6.8, at 37°C. Brains were post-fixed for at least 48 hours. Coronal sections (50 µm thick) were obtained using a vibratome and were treated for 15 min with 0.1% NaBH₄ in cytoskeletal buffer containing (in mM): NaCl 130, MES 10, EGTA 5, MgCl₂ 5, Glucose 5, pH adjusted to 6.3. After one-hour incubation with 10% normal goat serum in PBS containing 0.3% Triton-X, sections were washed and incubated for 24 hours at 4°C with primary antibodies diluted in PBS containing 0.3% Triton-X. For incubation with primary antibody against GLT1, 5% normal goat serum was added to the primary antibody solution. Following washes with PBS, sections were incubated for two hours with fluorescently labelled secondary antibodies, mounted in ProLong Gold Antifade reagent (Life Technologies), and imaged using LSM 880 with AiryScan (Zeiss).

The images presented in the figures illustrate the middle parts of the SON and the magnocellular PVN, at anterior-posterior bregma coordinates -0.90 to -1.00 mm for the SON, and -1.70 to -1.80 mm for the PVN. The morphology of the SON and PVN appears different, specifically, both nuclei are bigger with more prominent VP neuron population and angiogenesis due to the previously characterized phenomenon referred to as hypertrophy, that takes place in these nuclei in response to HSD. 9,93,94

Antibodies

Primary antibodies used were vasopressin guinea pig polyclonal antibody (SYSY 403004, 1:500), oxytocin mouse monoclonal antibody (PS38, 90 1:100; provided by Dr. Hal Gainer, NIH), GFAP chicken polyclonal antibody (Abcam ab4674, 1:1000), Iba1 (Ionized calcium-binding adaptor molecule 1) rabbit polyclonal antibody (WAKO 019-19741, 1:500), Iba1 guinea pig polyclonal antibody (SYSY 234-004, 1:500), CD68 mouse monoclonal antibody (Biorad MCA341GA, 1:500), S100β rabbit monoclonal antibody (Abcam ab52642, 1:500), ALDH1L1 rabbit polyclonal antibody (Proteintech 17390-1-AP, 1:50), GLT1 rabbit polyclonal antibody (Abcam ab106289, 1:500), vimentin mouse monoclonal antibody (DSHB 40ECs, 1:100), TMEM119 rabbit polyclonal antibody (SYSY





400203, 1:400), NeuN (or hexaribonucleotide binding protein-3a) guinea pig polyclonal antibody (Millipore Sigma ABN90, 1:200). Secondary antibodies used were Alexa-conjugated IgG (405 nm, 488 nm, 568 nm, and 647 nm; 1:500, Invitrogen) and DAPI (1:5000, Invitrogen).

Confocal microscopy with AiryScan

Confocal microscopy was conducted using LSM 880 with Apo 20x/0.8 objective (Zeiss), and AiryScan imaging was carried out using Zeiss 63x/1.40 Oil DIC f/ELYRA objective. For the super-resolution imaging, the AiryScan super-resolution (SR) module with 32-channel hexagonal array GaAsP detector for LSM (Zeiss) was used to collect stacks of 100-150 optical sections (170-nm step) using imaging parameters as we previously described. The point spread functions (PSFs) were measured and the maximal resolution of the Airyscan system at the wavelength used for CD68 imaging (excitation of 488 nm) was 126 nm in the lateral (xy) dimension and 346 nm in the axial (z) dimension. AiryScan super-resolution image stacks were reconstructed using ZEN Black software (Zeiss). Images were analyzed using ZEN Blue software (Zeiss) and FIJI (NIH).

Confocal live imaging in acute sections

Adult Sprague Dawley rats (300-400 g) expressing eGFP under the lba1 promoter were stereotaxically injected with adeno-associated virus serotype 6 (AAV6), which has a higher affinity for astrocytes. AAV6 were designed to express the fluorescent reporter tdTomato under the astrocyte-specific promoter gfaABC1D (AAV6-gfaABC1DtdTomato). The viruses were constructed by Canadian Neurophotonics Platform Viral Vector Core Facility (RRID:SCR_016477). Three weeks after stereotaxic surgery, rats were euthanized by decapitation, and their brains were rapidly extracted and placed in ice-cold sucrose solution containing (in mM): 252 sucrose, 2.5 KCl, 2 MgCl₂, 1.5 CaCl₂, 1.25 NaH₂PO₄, 26 NaHCO₃, and 10 D-glucose; pH 7.35; 300 mOsmol/kg, bubbled with carbogen (95% O₂ and 5% CO₂). Acute angled horizontal slices (350 μ m thick) were prepared as described previously and placed in a recording chamber on a microscope equipped with a 25X/0.95 NA water immersion objective (Leica SP8). Slices were continuously perfused at 1.5 ml/min with warm oxygenated (95% O₂; 5% CO₂; 31.5 ± 1°C) artificial cerebrospinal fluid (aCSF) for \sim 60 minutes before imaging. The aCSF comprised (in mM) 113 NaCl, 24 NaHCO₃, 1.25 NaH₂PO₄, 2.5 KCl, 1 MgCl₂, 2 CaCl₂, 10 D-glucose, osmolality 300 mOsmol/kg. For hypertonic aCSF, additional 20 mM of manitol was added for the osmolality 320 mOsmol/kg, a value comparable to the blood osmolality of rats fed HSD. ^{53,91,92} eGFP and tdTomato were visualized by time-lapse imaging of confocal z-stacks consisting of 10 optical planes (5 μ m step), acquired every 20 seconds. Slices were imaged for 15 minutes under baseline conditions (perfusion with control 300 mOsmol/kg aCSF), after which perfusion was switched to hypertonic 320 mOsmol/kg aCSF.

Image analysis and quantification

For the glia coverage analysis, $50 \, \mu m$ -thick brain sections containing SON or PVN were imaged as z-stacks ($1 \, \mu m$ step, 20x objective). Maximal intensity projection images were generated and the SON or PVN area containing VP neurons was identified by outlining the location of VP-positive cells. Then, the total immunopositive area for Iba1 or GFAP overlapping with the location of VP neurons was calculated using FIJI. Microglia density was calculated by counting the number of Iba1-positive cells in a $100 \, \mu m \times 100 \, \mu m$ area positioned over a central region of VP-positive area in the SON or PVN.

The intensity of $S100\beta$, ADLH1L1, GLT1, and vimentin in the SON is presented as a percentage relative to the area outside the SON. The relative intensity was calculated by dividing the total intensity of the SON VP-positive area by the total intensity of the adjacent VP-negative area outside the SON.

The total number of astrocytes in the SON and PVN was calculated by counting the number of S100β-positive cells within the area outlined by the location of VP-positive cells in the SON or the magnocellular part of the PVN. Astrocyte density in the SON and PVN was calculated by dividing the total number of S100β-positive cells by the VP-positive corresponding area.

For analysing microglia morphology, brain sections labeled for the VP, lba1, and DAPI, z-stacks (60-100 optical sections, 0.5 µm step, 63x objective) were imaged. Microglia shape was analysed in animals from different experimental groups, comparing morphology of lba1-positive cells located within the area containing VP neurons and outside the SON and PVN. The microglia complexity and process ramification were evaluated by calculating the number of Sholl intersections as a function of the distance from the microglial soma. For the generation and comparison of Sholl distribution curves, individual microglia Sholl profiles were generated, and profiles of 20 cells were averaged per rat. ⁹⁶ Each data point represents a mean value calculated for 5 rats per condition (Figure 2D). Incompletely stained microglia were not included in the analysis.

For the CD68 lysosome quantification, z-stacks containing the whole microglia soma were acquired using AiryScan super-resolution mode (150 nm step, 63x objective, zoom 2x). Maximal projection images were generated, and the area occupied by CD68 positive lysosomes was calculated for an individual microglia soma as a ratio between total CD68+ area and the total lba1-positive area. FIJI 3D reconstruction of lba1-positive microglia was used to identify and quantify the location of astrocytic and neuronal markers inside phagocytic lysosomes. Then, the number of CD68+ lysosomes, CD68/GFAP-double positive lysosomes, CD68/NeuN-double positive lysosomes, and CD68/VP-double positive lysosomes were counted for individual microglia.

IMARIS 3D Reconstruction of microglia were done by converting raw czi stacks of to the ims format in IMARIS software (Version 10.1.1, Oxford Instruments). Image processing was used to remove background noise prior to reconstruction by applying baseline subtraction to the Iba1 channel. Microglia and lysosomes were reconstructed using the surfaces tool by using the smooth function





followed by absolute intensity thresholding. For astrocytic proteins (GFAP and S100β), the thresholding was performed using background subtraction (local contrast). Videos were made in the Animation window and images of the reconstructed microglia were taken using the Snapshot tool.

Administration of microglia inhibitors

PLX3397 (Cat.#HY-16749, MedChemExpress) was first diluted as a stock in dimethyl sulfoxide (DMSO, 100 mg/ml), sonicated, aliquoted, and stored at -80 °C. Prior to the drug administration, the stock was diluted to prepare the injecting solution in the final concentration of 10 mg/ml in 10% DMSO, 40% PEG300, 5% Tween-80, and 45% saline. Rats (~300-350 g) were i.p. administered with 1 ml of the injection solution daily, for the final dose of 30 mg/kg/day. The control group received 1 ml of the vehicle containing 10% DMSO, 40% PEG300, 5% Tween-80, and 45% saline.

PLX5622 (Cat.#HY-114153, MedChemExpress) was first diluted as a stock in dimethyl sulfoxide (DMSO, 100 mg/ml), sonicated, aliquoted, and stored at -80 °C. Prior to the drug administration, the stock was diluted to prepare the injecting solution in the final concentration of 6.5 mg/ml in 10% DMSO, 20% RH40 (KolliphorR RH40, Sigma), 5% Tween-80 and 65% saline. Rats (~300-350 gr) were i.p. administered with 2.7 ml of the injection solution twice a day, for the final dose of 100 mg/kg/day. The control group received 2.7 ml of the vehicle containing 10% DMSO, 20% RH40, 5% Tween-80, and 65% saline.

BLZ945 (Cat.#HY-12768, MedChemExpress) was dissolved as a stock in DMSO at the concentration of 60 mg/ml and stored at -80 °C. Then, 2 ml of the stock solution was mixed with 4 ml of PEG300, and the total 6 ml solution (final concentration of 20 mg/ml) was injected i.c.v. into rats daily. The control group received 6 μ l of the vehicle containing 2 μ l DMSO and 4 μ l PEG300 daily. Rats were installed with i.c.v. cannulas \sim 2 weeks prior to the first BLZ945 or vehicle injection, and i.c.v. injections were done in awake freely moving rats.

All the drugs or vehicles were administered for 3 days prior to introducing rats to HSD or control diet, and drug or vehicle administration continued during the entire period when rats were exposed to control or HSD. Both i.p. and i.c.v. drug and vehicle administrations were performed in awake rats. To habituate them to the procedure, the rats were handled for 5 days prior to the first manipulation.

Acute hypothalamic slice preparations

VP-eGFP rats were euthanized by decapitation and brains were isolated and kept in an ice-cold sucrose solution containing (in mM): 252 sucrose, 2.5 KCl, 2 MgCl₂, 1.5 CaCl₂, 1.25 NaH₂PO₄, 26 NaHCO₃, and 10 D-glucose; pH 7.35; 300–320 mOsmol/kg, bubbled with carbogen (95% O₂ and 5% CO₂). Acute angled horizontal slices (350 μm thick) were prepared as described previously⁹⁵ and placed in a recording chamber on a fixed-stage microscope equipped with a 40X water immersion objective (Zeiss examiner, Z1. AXIO, Zeiss). Slices were perfused at 1.5 ml/min with warm oxygenated (95% O₂; 5% CO₂; 31.5 ± 1°C) aCSF for 45 - 60 minutes before recording. The aCSF comprised (in mM) 113 NaCl, 24 NaHCO₃, 1.25 NaH₂PO₄, 2.5 KCl, 1 MgCl₂, 2 CaCl₂, 10 D-glucose, osmolality 297 ± 3 mOsmol/kg.

Whole-cell electrophysiology

For current clamp recordings to measure the neuronal excitability, the patch pipettes were filled with intracellular solution containing (in mM): 140 K-gluconate, 2.5 MgCl₂, 10 HEPES, 2 Na₂-ATP, 0.5 Na-GTP, and 0.5 EGTA; pH 7.3, 285–295 mOsm/kg. Pipette resistance in the bath was 3–4 M Ω and recordings were excluded if the RMP was more positive than -50 mV or series resistance was >25 M Ω . Baseline activity was recorded in aCSF for at least 15 minutes before a drug application of glutamate transporter 1 (GLT1) inhibitor dihydrokainic acid (DHK 100 μ M, Sigma) or NMDAR subunit NR2B antagonist ifenprodil (10 μ M, Sigma).

For voltage clamp recordings to measure the NMDA receptor-mediated tonic current, the patch pipettes were filled with an intracellular solution containing (in mM): 135 cesium methane-sulphonate, 0.2 EGTA, 10 HEPES, 1 MgCl₂, 2 MgATP, 0.2 NaGTP, 10 TEA-CI, and 20 sodium phosphocreatine; pH 7.25 ± 0.05 . The low magnesium ACSF used in recording NMDA currents comprised (in mM): 113 NaCl, 24 NaHCO₃, 1.25 NaH₂PO₄, 2.5 KCl, 1 MgCl₂, 2 CaCl₂, 10 D-glucose, and 0.001 tetrodotoxin (TTX, Alomone labs, Israel), osmolality 297 \pm 3 mOsmol/kg.

The NMDA receptor-mediated tonic current (tonic I_{NMDA}) was assessed as changes in the holding current ($I_{holding}$). The mean tonic I_{NMDA} amplitude was calculated by the difference in $I_{holding}$ measured as the average of a 2 min steady-state baseline segment obtained before and 5 min after the application of NMDAR antagonists (ifenprodil 10 μ M, AP-5 100 μ M, and kynurenic acid 1mM, Sigma). I_{NMDA} was recorded and calculated at voltage clamped potential +40 mV.

The data were acquired with pCLAMP 11.0 (Molecular Devices) at a sampling rate of 10-20 kHz and measured and plotted with pCLAMP 11.0. A custom written Matlab script was used for to generate action potential raster plots. Prism (GraphPad Prism 9.1.0) was used to generate histogram distributions.

Blood pressure monitoring

Blood pressure was monitored by recording arterial blood pressure and heart rate in conscious unrestrained adult rats using radio telemetry as previously described.⁵³ Adult Wistar rats were anesthetized with isoflurane (induction: 4%, maintenance: 1–2%), and administered with Buphrenorphine (0.05 mg/kg), VetPen 300 (penicillin 1x10⁵ IU/kg), and saline (50 ml/kg). The telemetry transmitter (PTA-M/F FLAT, Stellar Telemetry, TSE Systems) was placed and secured in a subcutaneous pocket on the back of the animal. The





attached indwelling catheter with the blood pressure sensor was inserted into the femoral artery and advanced into the abdominal aorta. The systolic and diastolic arterial pressure, heart rate, and body temperature were sampled at 100 Hz for 15-second periods every 30 min. The telemetry sensors wirelessly communicated with an external antenna (Stellar Telemetry, TSE Systems), and the transmitted parameters were recorded by AcqKnowledge BIOPAC software. For the i.c.v. drug administration, 2 weeks after recovery from telemetry implantation surgery, rats were subjected to intracerebroventricular cannula implantations. Blood pressure measurements were initiated a week before treatment onset, to establish baseline arterial pressure values. At the end of dietary and pharmacological protocols, telemetry devices were extracted, and rat brains were fixed to confirm the position of the cannula and evaluate the effects of the treatments.

Western Blot

Tissue blocks containing the SON were removed and homogenized in ice-cold lysis buffer consisting of 200 mM HEPES, 50 mM NaCl, 10% glycerol, 1% triton X-100, 1 mM EDTA, 50 mM NaE, 2 mM Na₃VO₄, 25 mM β-glycerophosphate, and 1 EDTA-free complete ULTRA tablet. A total of 40 μg of protein per sample was resolved on SDS-PAGE (10%), transferred onto nitrocellulose membranes, and imaged using a ChemiDoc Imaging System (BioRad). Primary antibodies for western blotting are GFAP (cat# G4546; Sigma-Aldrich), GLT1 (cat# ab106289; Abcam), ALDH1L1 (cat# 17390-1-AP, Proteintech), raised in rabbit, and β-actin (cat# a5441; Sigma-Aldrich) raised in mouse. Secondary antibody for western blotting is anti-rabbit and anti-mouse HRP (Invitrogen).

QUANTIFICATION AND STATISTICAL ANALYSIS

All analyses were performed using Prism (GraphPad 9.1.0). Results are reported as mean plus or minus standard error of the mean (\pm SEM). Data were assessed for normality and statistical tests were performed to compare group values using Prism. Data of two groups were compared by a two-tailed, unpaired, parametric Student's t-test. For parametric multiple comparisons, we used one-way ANOVA followed by between-group comparisons using Tukey's post hoc test, or a repetitive measured (RM) two-way ANOVA followed by between-group multiple comparison Tukey's or Šídák's multiple comparisons post-hoc test. Differences between values considered statistically significant at p < 0.05; *p < 0.05, **p < 0.01, ***p < 0.001, ****p < 0.0001.

All the analyses, including statistical tests, multiple comparison post-hoc tests (if applicable), and p values for all groups compared in multiple comparisons, are summarised in Table S2.